animals were fed a laboratory rodent diet (CE-2; CLEA Japan) and given water *ad libitum*. All experimental protocols involving rats in this study were reviewed and approved by the Institutional Animal Care and Use Committee of the National Institute of Radiological Sciences (NIRS) and were performed in strict accordance with the NIRS Guide for Care and Use of Laboratory Animals.

Mating. Female F344 rats were monitored for the stage in their estrous cycle. Pro-estrous or estrous females were placed with an individually housed male Eker rat ($Tsc2^{+/-}$) overnight. Pregnancies were dated from gestational day 0 (GD0), being the day after mating.

Radiation exposure. Pregnant F344 rats, at GD15 and GD19, and F1 rats, at postnatal day 5 (PND5), PND20, and PND49, were whole-body irradiated with 0.5 or 2 Gy of ^{137}Cs gamma irradiation at the dose rate of 0.7 Gy/min. Exposure to gamma rays was conducted using a Gammacell 40 (Atomic Energy of Canada, Ottawa, Canada).

Genotyping. At the time of weaning, we determined the genotype of all (F344 × Eker) F1 rats by PCR. An ear-punched tissue sample was incubated in 200 μL DirectPCR Lysis Reagent (Ear, Cat # 402-E; Viagen Biotech, LA, CA, USA) containing 0.2 mg/mL of proteinase K (Wako Pure Chemical Industries, Osaka, Japan) at 55°C for 6 h, then heated at 85°C for 45 min. After centrifugation, the supernatant was used as template DNA. To discriminate *Tsc2* mutant or wild-type allele the following primer sequences were used: 5MFJ, 5′-ACCATCAGGATGCTGCTGAA-3′; 3MFJ2, 5′-CTATGGCCACATGTGACCAA-3′; and TSR27, 5′-GCGCCAGATTCACCTCATTA-3′.

The PCR procedure consisted of the initial heating at 94°C for 5 min, followed by 35 cycles of 94°C for 1 min, 55°C for 1 min, and 72°C for 1.5 min. The PCR products for wild-type and mutant *Tsc2* alleles were visualized by 3% agarose gel electrophoresis in the presence of ethidium bromide. With 5MFJ and TSR27 primers, the presence of the mutant allele was detected as 129 bp product, and with 5MFJ, TSR27 and 3MFJ2 primers, not only 129 bp but also 204 bp product from wild-type allele were amplified.[22] Only (F344 × Eker) F1 rats with the genotype of $Tsc2^{+/-}$ were used in this study.

Pathology and immunohistochemistry. Both unirradiated and irradiated F1 rats ($Tsc2^{+/-}$) were killed humanely under ether anesthesia at 27 weeks of age. Kidneys were removed and fixed in 10% neutral buffered formalin at room temperature for 18–24 h, then transversely trimmed into five sections per kidney. These were embedded in paraffin and further sectioned to a thickness of 4 μm, then H&E stained for histologic evaluation for premalignant (phenotypically altered tubules [PAT] and atypical hyperplasia) and malignant (adenoma and adenocarcinoma) lesions.

For immunohistochemistry analysis, 4-μm sections were deparaffinized through graded ethanol series, rehydrated, and washed with Tris- buffered saline (TBS) containing 0.1% (w/v) Tween 20. Sections were then incubated overnight at 4°C with the following primary antibodies at the indicated dilution: (1) phospho-Akt1 (Thr308) (ab66134) rabbit pAb (1:50) (Abcam,

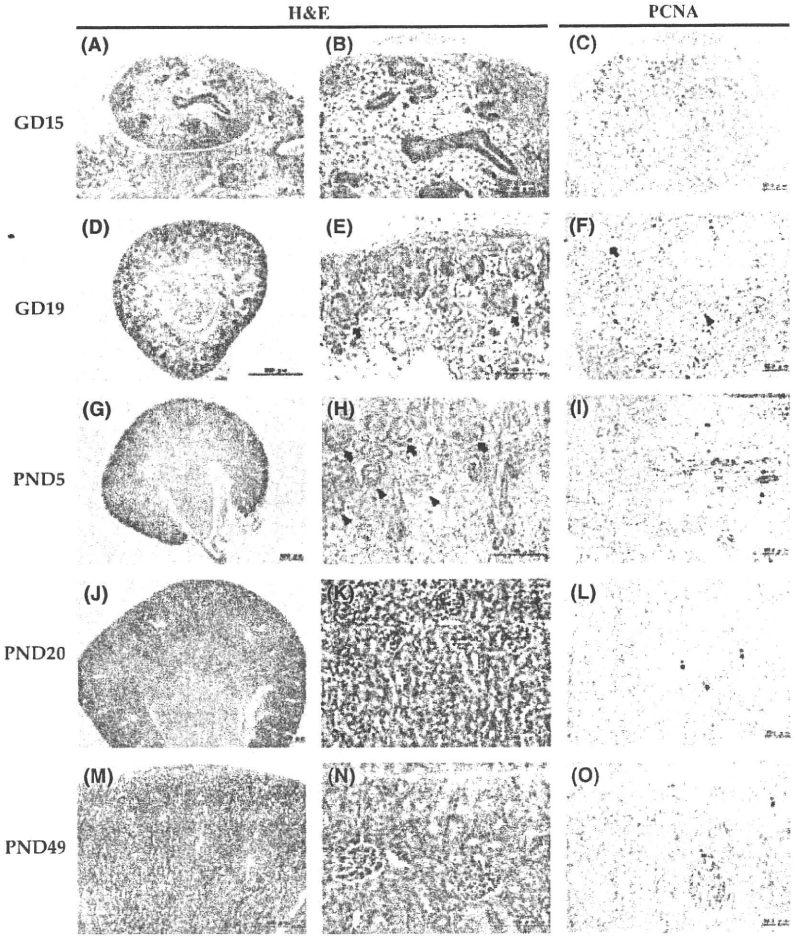

Fig. 1. Development of the kidney in (F344 × Eker) F1 rats. Tissue sections of kidneys from rats irradiated at gestational day 15 (GD15) (A–C), GD19 (D–F), postnatal day 5 (PND5) (G–I), PND20 (J–L), or PND49 (M–O) are shown. Panels on the middle show an enlarged field taken from each panel on the left. Panels on the left and the middle are H&E stained. Panels on the right show the proliferating cell nuclear antigen (PCNA) immunostaining. At GD15, the kidney consists of ureteric epithelium cells and undifferentiated mesenchymal cells. These cells are strongly positive for PCNA staining. At GD19, the typical S-shaped bodies (arrows) and glomeruli (arrow head) appear. They are also positive for PCNA staining. At PND5, a multitude of S-shaped bodies and glomeruli in an inner cortex and tubules extending into the medulla are positive for PCNA. At PND20, The nephrons develop into the structures similar to those in adults. The number of PCNA positive cells decrease and only a few cells are positive (asterisks). At PND49, nephrogenesis is mostly completed. The positive PCNA cells are rarely observed. Arrows and arrowheads indicate S-shaped body and the glomerulus, respectively.

Cambridge, UK); (2) phospho-mTOR (Ser2448) (49F9) rabbit mAb (1:50) (Cell Signaling Technology, Beverly, MA, USA); (3) phospho-S6 ribosomal protein (Ser235/236) (91B2) rabbit mAb (1:75) (Cell Signaling Technology); (4) phospho-4E-BP1 (Thr37/46) (236B4) rabbit mAb (1:400) (Cell Signaling Technology); and (5) proliferating cell nuclear antigen (PCNA) (PC10) mouse mAb (1:50) (Dako, Glostrup, Denmark). Antibody binding was detected by the avidin–biotin complex (ABC) method of staining using a Vectastain Elite ABC kit (PK-6101; Vector Laboratories, Burlingame, CA, USA) except for PCNA, for which the Dako EnVison Plus HRP system (K4006) was used following the manufacturer's protocol.

LOH and mutation analysis. Serial paraffin sections (4-μm thick) of renal tumor tissues were mounted on a polyethylene terephthalate membrane slide (Molecular Machines & Industries, Glattbrugg, Switzerland) and stained with H&E. Selected tissues (adenoma or adenocarcinoma) were microdissected using laser microdissection equipment (mmi CellCut system; Molecular Machines & Industries). Genomic DNA was then extracted from the tissue after proteinase K treatment (QIAamp DNA Micro kit; Qiagen, Hilden, Germany). LOH at the *Tsc2* allele was detected by PCR using the following primers: 5MFJ, 3MFJ2, and TSR27.[22] LOH at D10RAT91 and D10RAT47 neighboring *Tsc2* locus was detected using the primer sets of 5′-TGGGAACATTGTACCACTGTG-3′ and 5′-TCCCTG-AGGGGCTTTCTAGT-3′, and 5′-TCACAATTCTCCACG-TGAGG-3′ and 5′-TTTTTCCCCTTCTTTCTGACTG-3′, respectively. The PCR amplification program was as follows: 94°C for 9 min, then 45 cycles of 94°C for 30 s, 60°C for 1 min, and 72°C for 1 min. 5MFJ and 3MFJ2 were located in *Tsc2* intron 31, and TSR27 was located in the Eker insertion at intron 31. The microsatellite markers D10RAT91 and D10RAT47 (located at the 5′- and 3′-flanking regions of *Tsc2* at a distance of 4.1 Mbp and 2.2 Mbp, respectively) were also used for LOH determination (UCSC Genome Browser on Rat Nov. 2004 Assembly). The PCR amplification program used was: 94°C for 9 min, 45 cycles of 94°C for 30 s, 54°C for 30 s, 72°C for 30 s, and a final extension at 72°C for 5 min. The PCR products were separated on 4% agarose gel containing ethidium bromide.

Statistical analysis. The incidence and multiplicity of premalignant and malignat lesions between unirradiated and irradiated groups were analyzed using the Wilcoxon test. Increase in the percentage of phosphoryalted Akt positive cells within the tumors compared to surrounding normal tubules were also examined by the Wilcoxon test. Values of $P < 0.05$ were considered statistically significant.

Results

Development of the kidney in (F344 × Eker) F1 rats. We first examined normal development of the kidney in unirradiated F1 hybrid rats. The adult kidney originates from the metanephros, and its development is initiated in fetuses at GD12. At GD15, the immature kidney shows an outer zone, consisting of undifferentiated mesenchymal and ductal epithelial cells, undergoing mesenchymal and epithelial transitions (Fig. 1A,B). Both types of cells are actively proliferating, as revealed by strong PCNA staining (Fig. 1C). At GD19, the kidney has a peripheral zone of nephrogenic mesenchyme, a cortex containing numerous immature nephron structures, and a medulla with interstitial cells (Fig. 1E,F). The typical comma- and S-shaped bodies appear in the subcapsular layer, which are destined to develop into distal and proximal tubules, Henle's loop, collecting ducts, and glomerular podocytes.[23,24] At PND5, S-shaped bodies are still abundant in the subcapsular layer, glomeruli appear in the cortex, and tubules within the medullary rays have developed extensively (Fig. 1G,H). Tubular growth is a feature of the outer medullary region and is associated with interstitial spaces. At PND5, not only S-shaped bodies but also tubules extending into the medulla are intensely stained with PCNA (Fig. 1I). At PND20, the kidneys achieve their adult zonation, that is a cortex, outer medulla, and inner medulla (Fig. 1J,K); developing loops of Henle and interstitial cells in the medulla are still positive for PCNA (Fig. 1L). At PND49, nephrogenesis is mostly completed, the functional glomerulus has grown in size, and distal and proximal tubules have further elongated (Fig. 1M,N). In addition, PCNA-positive cells are detectable, scattered in the proximal and distal tubules (Fig. 1O). As a whole, the developmental pattern of F1 hybrid rats was quite consistent with that previously reported.[24–26]

Pathology of renal tubular lesions. F344 female rats were mated with Eker male rats heterozygous for *Tsc2* ($Tsc2^{+/-}$) and were irradiated with gamma rays at 0.5 or 2 Gy on GD15, GD19, PND5, PND20, and PND49. All F1 rats were sacrificed at 27 weeks of age and examined for kidney lesions. Renal

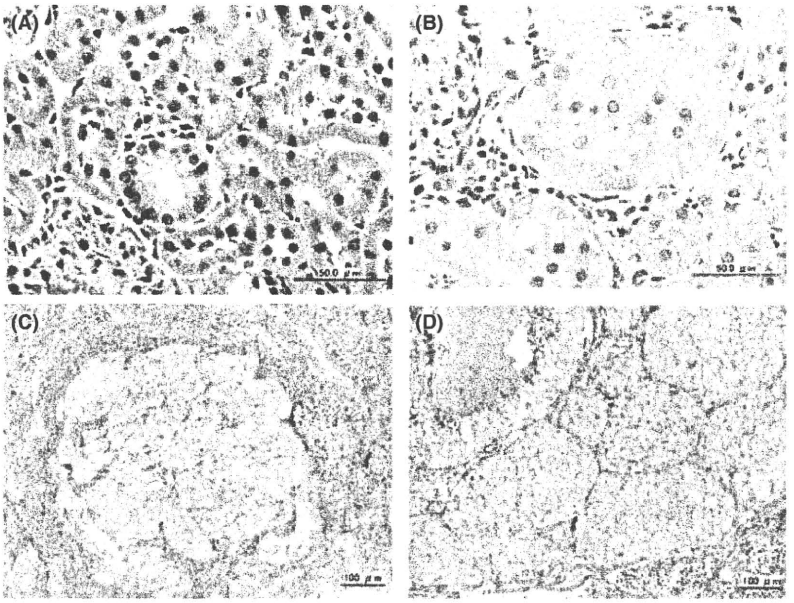

Fig. 2. Tissue sections (H&E stained) showing radiation-induced lesions in a kidney from a 27-week-old F1 rat. (A) Phenotypically altered tubule; (B) atypical hyperplasia; (C) adenoma; (D) adenocarcinoma.

doi: 10.1111/j.1349-7006.2009.01456.x

epithelial lesions were first identified as PAT (phenotypically altered tubules), which showed a single layer of altered or swollen cells (Fig. 2A).[27] These progress to atypical hyperplasia, adenoma, and adenocarcinoma (Fig. 2).[28] Atypical hyperplasia are tubules filled with multiple layers of altered cells that occlude the lumen and expand the normal tubule size but remain smaller than three average tubules (Fig. 2B). Adenoma is characterized by focal proliferation and atypical epithelial-type tubular epithelium, with compression of the adjacent parenchyma (Fig. 2C). Adenocarcinoma is diagnosed compositely by a combination of the following features: (i) invasions into the surrounding kidney parenchyma; (ii) greater frequency of mitotic figures; (iii) presence of areas of hemorrhage or necrosis; and (iv) presence of pleomorphic or anaplastic cells (Fig. 2D). Pathologically, there was no difference between spontaneous and radiation-induced lesions.

Incidence and multiplicity of lesions and tumors. In male rats, irradiation with 0.5 Gy increased the multiplicity of PAT after GD19 (Table 1). Multiplicity was not increased by irradiation at GD15, however, when nephron structures had not yet developed. Irradiation with 2 Gy at GD19 or later increased the number of PAT as a function of age-at-irradiation. Increase in the incidence of atypical hyperplasia was evident by irradiation after GD15 or later. The kidneys of rats at GD15 were rather refractory to these

Table 1. Incidence and multiplicity of kidney lesions in male F1 rats after exposure to gamma radiation

	n	Findings					
		Phenotypically altered tubules		Atypical hyperplasia		Adenoma and adenocarcinoma	
		Incidence	Multiplicity	Incidence	Multiplicity	Incidence	Multiplicity
Unirradiated control (0 Gy)	16	16 (100)†	20.5 ± 9.2‡	10 (63)	1.7 ± 2.0	4 (25)	0.3 ± 0.6
0.5 Gy of gamma radiation							
Age at exposure							
GD15	13	13 (100)	16.8 ± 5.7	8 (50)	1.0 ± 1.4	6 (46)	0.7 ± 0.9
GD19	8	8 (100)	30.4 ± 13.7	7 (88)	2.0 ± 1.6	2 (25)	0.3 ± 0.5
PND5	10	10 (100)	37.0 ± 14.6**	10 (100)	4.5 ± 1.8**	1 (10)	0.2 ± 0.6
PND20	11	11 (100)	33.8 ± 11.7**	7 (64)	1.5 ± 1.6	3 (27)	0.4 ± 0.7
PND49	9	9 (100)	34.4 ± 14.4*	6 (67)	1.7 ± 2.0	4 (44)	0.4 ± 0.5
2 Gy of gamma radiation							
Age at exposure							
GD15	6	6 (100)	20.0 ± 11.4	6 (100)	4.7 ± 2.8*	5 (83)*	1.6 ± 1.4**
GD19	9	9 (100)	28.1 ± 10.1*	9 (100)	14.9 ± 5.4**	9 (100)**	4.0 ± 2.2**
PND5	6	6 (100)	34.2 ± 16.0*	6 (100)	23.0 ± 9.8**	5 (83)*	1.7 ± 1.5*
PND20	8	8 (100)	49.9 ± 12.3**	8 (100)	19.5 ± 9.5**	4 (50)	0.8 ± 1.0
PND49	8	8 (100)	65.3 ± 10.7**	8 (100)	14.1 ± 6.6**	4 (50)	0.5 ± 0.5

*$P < 0.05$ compared to control. **$P < 0.01$ compared to control. †Percentage incidence shown in parentheses; ‡data presented as mean ± SD values. GD, gestational day; PND, postnatal day.

Table 2. Incidence and multiplicity of kidney lesions in female F1 rats after exposure to gamma radiation

	n	Findings					
		Phenotypically altered tubules		Atypical hyperplasia		Adenoma and adenocarcinoma	
		Incidence	Multiplicity	Incidence	Multiplicity	Incidence	Multiplicity
Unirradiated control (0 Gy)	17	17 (100)†	44.7 ± 14.9‡	13 (76)	3.1 ± 3.2	3 (18)	0.2 ± 0.6
0.5 Gy of gamma radiation							
Age at exposure							
GD15	12	12 (100)	34.1 ± 8.3*	7 (58)	1.8 ± 2.1	5 (42)	0.6 ± 0.8
GD19	8	8 (100)	49.5 ± 12.0	6 (76)	2.0 ± 2.1	5 (63)*	0.9 ± 0.8*
PND5	10	10 (100)	42.9 ± 7.1	7 (70)	1.2 ± 1.1	3 (30)	0.3 ± 0.5
PND20	8	8 (100)	44.1 ± 16.8	6 (75)	2.0 ± 1.9	3 (38)	0.4 ± 0.5
PND49	8	8 (100)	32.3 ± 9.0*	3 (38)	0.4 ± 0.5*	4 (50)	0.9 ± 1.4
2 Gy of gamma radiation							
Age at exposure							
GD15	8	8 (100)	37.3 ± 12.2	8 (100)	7.8 ± 6.2*	6 (75)**	1.0 ± 0.8*
GD19	7	7 (100)	33.7 ± 10.3	7 (100)	17.0 ± 7.4**	6 (86)**	1.6 ± 0.5**
PND5	7	7 (100)	53.3 ± 14.6	7 (100)	19.9 ± 8.8**	3 (43)	0.6 ± 0.8
PND20	7	7 (100)	63.0 ± 24.6	7 (100)	17.0 ± 10.0**	1 (14)	0.1 ± 0.4
PND49	7	7 (100)	68.0 ± 13.3**	7 (100)	19.7 ± 12.9**	5 (71)*	0.9 ± 0.7*

*$P < 0.05$ compared to control. **$P < 0.01$ compared to control. †Percentage incidence shown in parentheses; ‡data presented as mean ± SD values. GD, gestational day; PND, postnatal day.

radiation-induced both preneoplastic lesions. An increase in the multiplicity of adenoma and adenocarcinoma was evident in animals irradiated with 2 Gy at GD15, GD19, and PND5, being highest in animals irradiated at GD19 (Table 1).

Female rats had twice the number of spontaneously developed preneoplastic lesions (both PAT and atypical hyperplasia) compared to male rats: the percentage of animals displaying PAT was 44.7% and 20.5%, and atypical hyperplasia, 3.1% and 1.7%, for female and males, respectively, indicating a gender difference (Tables 1,2). Irradiation of female rats at 0.5 Gy did not effectively induce premalignant lesions. The multiplicity of adenoma and adenocarcinoma was slightly higher than that of the control when irradiated at GD19 (Table 2). Irradiation at 2 Gy efficiently induced PAT when exposed postnatally. An increase in the multiplicity of hyperplasia was evident when administered at GD15 or later (Table 2). Multiplicity of adenomas and adenocarcinomas was significantly increased by irradiation at 2 Gy, and was the highest in animals irradiated at GD19, although again the effect was less pronounced in males (Tables 1,2). Unexpectedly, irradiation at 2 Gy at PND20 showed no stimulative effect on the development of adenoma and adenocarcinoma (Table 2). Interestingly, however, 2 Gy irradiation at PND49 resulted in an increased multiplicity of adenoma and adenocarcinoma compared with the no-irradiation control (Table 2).

In both male and female rats, there was a clear difference in the dependency of age-at-irradiation between preneoplastic lesions (PAT and hyperplasia) and tumors (adenoma and adenocarcinoma). The preneoplastic lesions were preferentially induced as a function of age-at-irradiation, whereas tumors were induced by perinatal irradiation.

LOH analysis. LOH analysis of the *Tsc2* allele was performed for microdissected paraffin-embedded tumors and normal kidney tissues derived from both control and irradiated male rats

Table 3. LOH for the *Tsc2* locus and immunodetection of mTOR-related phosphorylation in renal tumors from male F1 rats

Tumor	Age at exposure (2 Gy)	LOH			Immunohistochemistry			
		D10RAT91	*Tsc2*	D10RAT47	Phospho-Akt1	Phospho-mTOR	Phospho-S6 ribosomal protein	Phospho-4E-BP1
1-1	Unirradiated control	○†	○	○	+‘	+	+	+
1-2	Unirradiated control	○	○	○	+	+	+	+
2	Unirradiated control	●‡	○	○	ND††	+	+	+
3	Unirradiated control	○	○	○	+	+	+	+
4-1	GD15	○	○	○	+	+	+	+
4-2	GD15	○	○	○	+	+	+	+
5-1	GD15	○	○	○	+	+	+	+
5-2	GD15	○	○	○	+	+	+	+
6-1	GD15	○	○	○	–	+	+	+
6-2	GD15	○	○	○	–	+	+	+
7-1	GD15	○	○	○	+	+	+	+
7-2	GD15	○	○	○	ND	+	+	+
7-3	GD15	○	○	○	+	+	+	+
7-4	GD15	○	○	○	ND	+	+	+
8-1	GD15	○	○	○	ND	+	+	+
8-2	GD15	○	○	●	ND	+	+	+
8-3	GD15	○	○	●	ND	+	+	+
9	GD19	○	○	○	ND	+	+	+
10-1	GD19	○	○	○	ND	ND	ND	ND
10-2	GD19	●	○	▲	+	+	+	+
11	GD19	▲§	●	●	+	+	+	+
12	GD19	●	○	●	ND	+	+	ND
13-1	GD19	●	○	○	ND	+	+	+
13-2	GD19	○	○	○	+	ND	ND	ND
14	GD19	●	○	○	+	+	+	+
15	GD19	●	●	●	ND	+	+	+
16	GD19	○	○	○	+	+	+	+
17	PND5	○	●	○	+	+	+	+
18	PND5	●	○	●	ND	+	+	+
19	PND5	●	○	○	+	+	+	+
20	PND20	○	○	●	ND	+	+	+
21-1	PND20	○	○	○	+	+	+	+
21-2	PND20	○	○	○	+	+	+	+
21-3	PND20	○	○	○	+	+	+	+
22	PND20	▲	●	●	ND	+	+	+
23	PND49	●	○	○	+	+	+	+
24-1	PND49	●	●	●	ND	+	ND	+
24-2	PND49	●	○	○	ND	ND	ND	ND
25	PND49	○	●	●	ND	ND	+	+
	Total	33.3 (13/39)	15.4 (6/39)	28.2 (11/39)				

†Retention of heterozygosity; ‡LOH (wild-type allele; F344 rat); §LOH (mutant type allele; Eker rat); ‘positive staining. ††Not determined due to of limited availability of tissue. GD, gestational day; mTOR, mammalian target of rapamycin; ND, not determined; PND, postnatal day.

doi: 10.1111/j.1349-7006.2009.01456.x

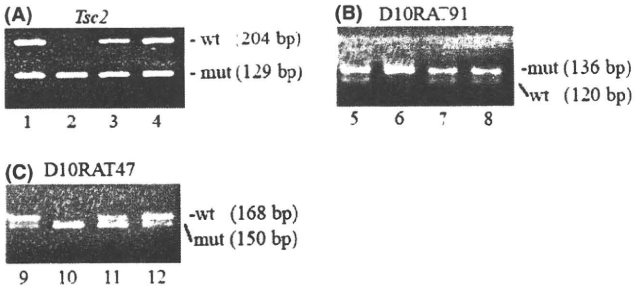

Fig. 3. Loss of the wild-type *Tsc2* allele and microsatellites in renal tumors from F1 rats. Representative results of LOH analysis are shown for *Tsc2* (A) and the microsatellite markers D10RAT91 (B) and D10RAT47 (C). Lanes: 1, 5, and 9, DNA from an F1 rat ear; 2, 6, and 10, microdissected renal tumor; 3, 7, and 11, microdissected normal kidney tissue; 4, 8, and 12, microdissected spleen tissue. In (A), wt and mut indicate wild-type and mutant *Tsc2* allele, respectively. In both (B) and (C), wt and mut indicate the allele of the wild-type rat (F344 rat) and Eker rat, respectively.

(Table 3 and Fig. 3). The LOH frequency was 15.4% as a whole. Specifically, there were no LOH-positive cases among the tumors from unirradiated controls (0/4) nor from rats irradiated at GD15 (0/13). For rats irradiated at GD19, PND5, PND20, and PND49, LOH was found in two of 10, one of three, one of five, and two of four tumors, respectively (Table 3). LOH frequency in tumors from rats irradiated at GD19 or later was 27% (6 of 22). This indicates that LOH at the *Tsc2* locus was induced by irradiation at GD19 and thereafter, but the frequency of LOH was relatively low. This frequency is comparable to that in renal tumors from Eker rats irradiated with 9 Gy at 4 weeks after birth (29%).[29] LOH at the flanking loci, D10RAT91 and D10RAT47, was unexpected; the frequency of LOH was almost twice as high as that at the *Tsc2* allele. Because the tumor samples were too small to analyze the *Tsc2* mutation, we could not determine if the remaining wild-type allele harbored small mutations.

Immunohistochemical analysis. Owing to a lack of molecular evidence of a *Tsc2* mutation, an immunohistochemical analysis was used to examine the status of the rapamycin-sensitive mTOR pathway, which is negatively regulated by the Tsc1/Tsc2 complex. With *Tsc2* deficiency, mTOR is activated and phosphorylates p70 S6 kinase and 4E-BP1. We found that the following three proteins were phosphorylated in all tumors, regardless of radiation dose, age at irradiation, and stage of malignancy: mTOR (Ser2448), an indicator of mTOR activation; S6 ribosomal protein (Ser235/236), a downstream substrate of p70 S6 kinase; and 4E-BP1 (Thr37/46) (Fig. 4). These results, showing activation of the mTOR pathway, suggest functional loss of *Tsc2* in LOH-negative tumors. We also examined the status of Akt, an upstream kinase that inactivates *Tsc2* protein product by direct phosphorylation. We observed positive staining of phosphorylated (i.e. activated) Akt in both nuclei and cytoplasm of the cells, not only in PAT but also in adenocarcinoma, whereas most normal tubules showed either negative staining or positive staining only in the nuclei (Fig. 4A). Then, we counted the number of cells of positive for phosphorylated Akt in 10 samples randomly selected from tumor and normal areas. The mean percentage of positive cells in normal and tumors area were $8.8 \pm 6.6\%$ and $77.3 \pm 8.8\%$ ($P < 0.01$), respectively, indicating that Akt was activated.

Discussion

We have shown that in renal carcinogenesis in (F344 × Eker) F1 rats ($Tsc2^{+/-}$): (1) preneoplastic PAT lesions increased after postnatal irradiation as a function of age-at-irradiation, and hyperplasia was greatly increased after perinatal and postnatal irradiation; (2) early development of adenoma/adenocarcinoma was evident when rats were irradiated at the perinatal stage, especially just before birth (GD19); and (3) the mTOR pathway was unexceptionally activated, which might reflect inactivation of *Tsc2*, in spite of low frequency of LOH at the *Tsc2* allele.

Large-scale cell proliferation and apoptosis have been observed during the normal development of fetal kidney in rats.[30] Mitotic indices were maximum at GD19 in the nephrogenic zone in the outer cortex, where S-shaped bodies were rapidly growing.[30] The cells in S-shaped bodies are destined to form not only glomeruli and proximal tubules but also the distal convoluted tubules, whereas the middle part grows into the loop of Henle. This structure is highly radiosensitive; massive, synchronous apoptosis is induced by irradiation.[31] This stage coincides with the susceptible age for radiation-induced renal adenoma and adenocarcinoma (Tables 1, 2). It is therefore likely that radiation initiates the cells in S-shaped bodies, and these expand selectively, in concert with an increase in the number of S-shaped bodies, to progress into more neoplastic tumors in the developmental microenvironment that is enriched with highly proliferative growth signals. The initiated cells in the postnatally differentiating renal tubules do not acquire malignancy by 27 weeks after birth, however, because of the low rate of proliferation. It has been reported that radiation-induced intestinal tumors in Min-mice are maximal for neonatal exposure but much lower for fetal exposure or adult exposure.[32] Crypts, where multi-potent stem cells and proliferating progenitor cells reside, are the basic structure for the development and maintenance of intestines. The number of crypts dramatically increases by fission after birth. It is thought that crypt stem cells initiated by radiation can rapidly increase in number during this developmental stage. The radiation sensitivity of two organs supports the idea that one of the important determinants for carcinogen susceptibility is the rate of increase in the number of stem cells. In humans, the S-shaped bodies are actively developing in fetal kidney at a gestational age of 20–34 weeks,[33] suggesting that fetuses at this age are at risk for radiation-induced renal carcinogenesis.

We observed that female rats are more predisposed to renal preneoplastic lesions than males (Tables 1,2). It has been reported that the rat kidney expresses a receptor for 17β-estradiol, and that estrogen up-regulates autocrine or paracrine polypeptide growth factor signaling such as transforming growth factor-α (TGF-α). In the absence of physiological estrogen as a consequence of ovariectomy, the development of lesions, especially PAT and hyperplasia, is inhibited.[34] Estrogen may therefore act in concert with overexpressed TGFα to promote the development of early lesions in Eker kidneys. Development of adenoma and adenocarcinoma is influenced little by ovariectomy, however.[34] Our data indicate that the incidence of adenoma and adenocarcinoma induced by irradiation at 2 Gy is more prevalent in males compared to females. Taken together, the progression of benign renal lesions into malignant lesions after irradiation depends on factors other than estrogen.

LOH is frequently observed in intestinal tumors for irradiated Apc1638N mice and in lymphomas for irradiated $p53^{+/-}$ mice, at 55% and 85%, respectively.[35,36] We observed, however, that the frequency of LOH at the *Tsc2* locus was unexpectedly low, at 15%. Nonetheless, downstream mTOR was unexceptionally activated. There may be several possible explanations. First, heterozygous *Tsc2* status is enough to induce kidney tumors, indicating haploinsufficiency. Tubers of patients with tuberous sclerosis complex (TSC) infrequently exhibit LOH for either *TSC1* or *TSC2*.[37] Angiomyolipomas, which are found in the kidney of 67% of TSC patients, do not always show LOH of *TSC1* or *TSC2*. Henske *et al.* failed to observe LOH in 21 of 53 renal angiomyolipomas.[38] Moreover, angiomyolipomas that do

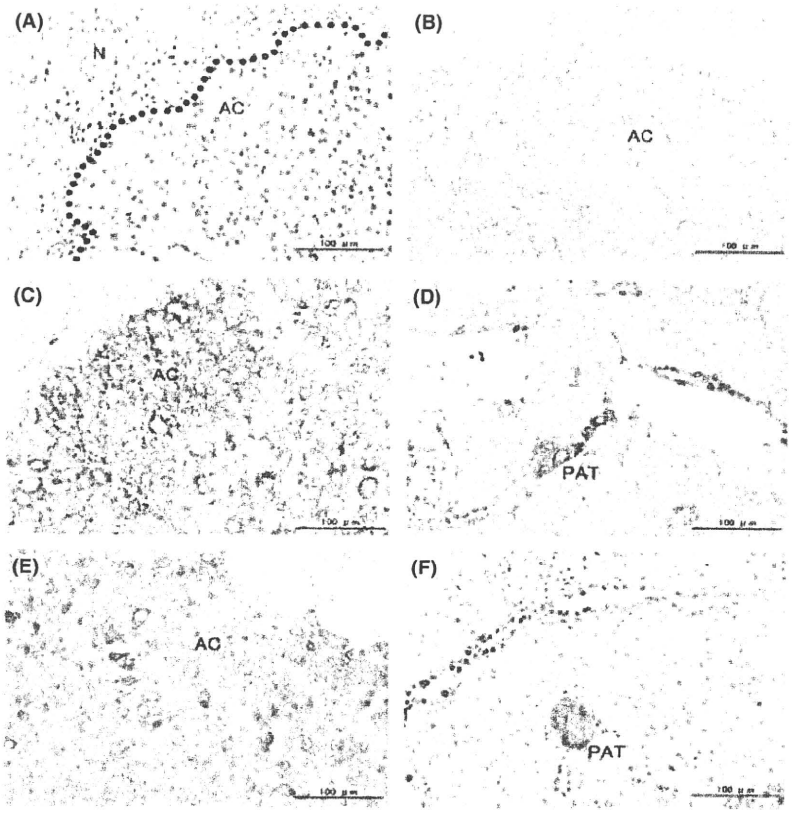

Fig. 4. Immunohistochemical analysis of renal lesions. Tissue sections of rat kidney were deparaffinized and incubated with the indicated mAb, then subjected to the avidin–biotin complex (ABC) method of staining. (A) Phospho-Akt1 (Thr308)-positive adenocarcinoma; (B) phospho-mTOR (Ser2448) positive adensocarcinoma; (C) phospho-S6 (Ser235/236)-positive adenocarcinoma; (D) phospho-S6 (Ser235/236)-positive phenotypically altered tubule; (E) phospho-4E-BP1 (Thr37/46)-positive adenocarcinoma; (F) phospho-4E-BP1 (Thr37/46) positive phenotypically altered tubule. AC, adenocarcinoma; N, normal tubules, PAT, phenotypically altered tubule.

not display LOH harbor no subtle second 'hit' mutation in *TSC1* or *TSC2*.[39] These findings suggest that an inactivating mutation of the second *TSC* allele is not necessary for TSC-lesion development in some cases. Evidence has been accumulated for haploinsufficiency of other tumor suppressor genes such as neurofibromatosis 1 (*NF1*),[40,41] phosphatase tensin homolog (*PTEN*),[42] and *p53*[43] in tumorigenesis. Furthermore, activation of other parts of the mTOR pathway may be involved. We demonstrated here that Akt was significantly phosphorylated in tumor lesions, and this may reflect the inactivation of Tsc2. Activated Akt may turn on the cascade of the mTOR pathway under the heterozygous *Tsc2* condition. Finally, it is more likely that there may exist small alterations, including deletions, duplications and point mutations, that cannot be detected by LOH analysis. It has been reported that renal carcinomas induced by *N*-ethyl-*N*-nitrosourea in Eker rats that were negative for LOH harbored point mutations. Intragenic somatic mutations such as deletions and duplications have been demonstrated in spontaneously developing renal carcinomas.[19] Point mutations and intragenic small deletions also have been demonstrated in radiation-induced renal carcinomas in Eker rats.[29] However, we could not determine the mutation status of the wild-type allele in the current study because the tumor samples were too small for that purpose.

In conclusion, the actively growing kidney is highly susceptible to radiation-induced renal cell carcinogenesis in prenatal (F344 × Eker) F1 rats, when the S-shaped bodies are extensively increasing in number, and this is accompanied by mTOR activation.

Acknowledgments

We thank Mr S. Tateno, Ms E. Kubo and all members of the Laboratory Animal Sciences Section of our institute for animal care. This work was supported by institute funds from the National Institute of Radiological Sciences, the LRI program of the Japan Chemical Industry Association, and a Grant-In-Aid for Cancer Research from the Ministry of Health, Labor and Welfare of Japan.

References

1 Choyke PL, Glenn GM, Walther MM, Zbar B, Linehan WM. Hereditary renal cancers. *Radiology* 2003; **226**: 33–46.
2 Pascual D, Borque A. Epidemiology of kidney cancer. *Adv Urol* 2008; doi: 10.1155/2008/782381.
3 Preston DL, Ron E, Tokuoka S *et al.* Solid cancer incidence in atomic bomb survivors: 1958–1998. *Radiat Res* 2007; **168**: 1–64.
4 Anderson LM, Diwan BA, Fear NT, Roman E. Critical windows of exposure for children's health: cancer in human epidemiological studies and neoplasms in experimental animal models. *Environ Health Perspect* 2000; **108** (Suppl 3): 573–94.
5 Wakeford R. Childhood leukaemia following medical diagnostic exposure to ionizing radiation in utero or after birth. *Radiat Prot Dosimetry* 2008; **132**: 166–74.
6 Bithell JF, Stewart AM. Pre-natal irradiation and childhood malignancy: a review of British data from the Oxford Survey. *Br J Cancer* 1975; **31**: 271–87.
7 Yoshimoto Y, Kato H, Schull WJ. Risk of cancer among children exposed in utero to A-bomb radiations, 1950–84. *Lancet* 1988; **2**: 665–9.
8 Ohaki Y. Renal tumors induced transplacentally in the rat by *N*-ethylnitrosourea. *Pediatr Pathol* 1989; **9**: 19–33.
9 Turusov VS, Alexandrov VA, Timoshenko IV. Nephroblastoma and renal mesenchymal tumor induced in rats by *N*-nitrosoethyl- and *N*-nitrosomethylurea. *Neoplasma* 1980; **27**: 229–35.
10 Dressler GR. The cellular basis of kidney development. *Annu Rev Cell Dev Biol* 2006; **22**: 509–29.
11 Diwan BA, Rice JM. Effect of stage of development on frequency and pathogenesis of kidney tumors induced in Noble (Nb) rats exposed prenatally or neonatally to *N*-nitrosoethylurea. *Carcinogenesis* 1995; **16**: 2023–8.

doi: 10.1111/j.1349-7006.2009.01456.x

12 Hino O, Mitani H, Knudson AG. Genetic predisposition to transplacentally induced renal cell carcinomas in the Eker rat. *Cancer Res* 1993; **53**: 5856–8.
13 Davies JA, Perera AD, Walker CL. Mechanisms of epithelial development and neoplasia in the metanephric kidney. *Int J Dev Biol* 1999; **43**: 473–8.
14 Gnarra JR, Ward JM, Porter FD *et al.* Defective placental vasculogenesis causes embryonic lethality in *VHL*-deficient mice. *Proc Natl Acad Sci U S A* 1997; **94**: 9102–7.
15 Laping NJ, Everitt JI, Frazier KS *et al.* Tumor-specific efficacy of transforming growth factor-βRI inhibition in Eker rats. *Clin Cancer Res* 2007; **13**: 3087–99.
16 Shiono M, Kobayashi T, Takahashi R *et al.* The G1556S-type tuberin variant suppresses tumor formation in tuberous sclerosis 2 mutant (Eker) rats despite its deficiency in mTOR inhibition. *Oncogene* 2008; **27**: 6690–7.
17 Kenerson H, Dundon TA, Yeung RS. Effects of rapamycin in the Eker rat model of tuberous sclerosis complex. *Pediatr Res* 2005; **57**: 67–75.
18 Hino O, Andres JPK-S, Jerome JF *et al.* Spontaneous and radiation-induced renal tumors in the Eker rat model of dominantly inherited cancer. *Proc Natl Acad Sci U S A* 1993; **90**: 327–31.
19 Kobayashi T, Urakami S, Hirayama Y *et al.* Intragenic *Tsc2* somatic mutations as Knudson's second hit in spontaneous and chemically induced renal carcinomas in the Eker rat model. *Jpn J Cancer Res* 1997; **88**: 254–61.
20 Inoki K, Corradetti MN, Guan KL. Dysregulation of the TSC-mTOR pathway in human disease. *Nat Genet* 2005; **37**: 19–24.
21 Al-Saleem T, Wessner LL, Scheithauer BW *et al.* Malignant tumors of the kidney, brain, and soft tissues in children and young adults with the tuberous sclerosis complex. *Cancer* 1998; **83**: 2208–16.
22 Fukuda T, Hirayama Y, Mitani H *et al.* Generation of metastatic variants of Eker renal carcinoma cell lines for experimental investigation of renal cancer metastasis. *Jpn J Cancer Res* 1998; **89**: 1104–8.
23 Moritz KM, Wintour EM, Black MJ, Bertram JF, Caruana G. Factors influencing mammalian kidney development: implications for health in adult life. *Adv Anat Embryol Cell Biol* 2008; **196**: 1–78.
24 Maric C, Ryan GB, Alcorn D. Embryonic and postnatal development of the rat renal interstitium. *Anat Embryol (Berl)* 1997; **195**: 503–14.
25 Marquez MG, Cabrera I, Serrano DJ, Sterin-Speziale N. Cell proliferation and morphometric changes in the rat kidney during postnatal development. *Anat Embryol (Berl)* 2002; **205**: 431–40.
26 Bertram JF, Young RJ, Spencer K, Gordon I. Quantitative analysis of the developing rat kidney: absolute and relative volumes and growth curves. *Anat Rec* 2000; **258**: 128–35.
27 Kubo Y, Klimek F, Kikuchi Y, Bannasch P, Hino O. Early detection of Knudson's two-hits in preneoplastic renal cells of the Eker rat model by the laser microdissection procedure. *Cancer Res* 1995; **55**: 989–90.
28 McDorman KS, Wolf DC. Use of the spontaneous *Tsc2* knockout (Eker) rat model of hereditary renal cell carcinoma for the study of renal carcinogens. *Toxicol Pathol* 2002; **30**: 675–80.
29 Hino O, Mitani H, Sakaurai J. "Second hit" of *Tsc2* gene in radiation induced renal tumors of Eker rat model. *Int Congr Ser* 2002; **1236**: 163–74.
30 Coles HS, Burne JF, Raff MC. Large-scale normal cell death in the developing rat kidney and its reduction by epidermal growth factor. *Development* 1993; **118**: 777–84.
31 Gobe GC, Axelsen RA, Harmon BV, Allan DJ. Cell death by apoptosis following X-irradiation of the foetal and neonatal rat kidney. *Int J Radiat Biol* 1988; **54**: 567–76.
32 Ellender M, Harrison JD, Kozlowski R, Szluinska M, Bouffler SD, Cox R. In utero and neonatal sensitivity of $Apc^{Min/+}$ mice to radiation-induced intestinal neoplasia. *Int J Radiat Biol* 2006; **82**: 141–51.
33 Takano K, Kawasaki Y, Imaizumi T *et al.* Development of glomerular endothelial cells, podocytes and mesangial cells in the human fetus and infant. *Tohoku J Exp Med* 2007; **212**: 81–90.
34 Wolf DC, Goldsworthy TL, Donner EM, Harden R, Fitzpatrick B, Everitt JI. Estrogen treatment enhances hereditary renal tumor development in Eker rats. *Carcinogenesis* 1998; **19**: 2043–7.
35 van der Houven van Oordt CW, Smits R, Williamson SL *et al.* Intestinal and extra-intestinal tumor multiplicities in the *Apc*1638N mouse model after exposure to X-rays. *Carcinogenesis* 1997; **18**: 2197–203.
36 Hong DP, Mori N, Umesako S *et al.* Putative tumor-suppressor gene regions responsible for radiation lymphomagenesis in F1 mice with different *p53* status. *J Radiat Res (Tokyo)* 2002; **43**: 175–85.
37 Tucker T, Friedman JM. Pathogenesis of hereditary tumors: beyond the "two-hit" hypothesis. *Clin Genet* 2002; **62**: 345–57.
38 Henske EP, Scheithauer BW, Short MP *et al.* Allelic loss is frequent in tuberous sclerosis kidney lesions but rare in brain lesions. *Am J Hum Genet* 1996; **59**: 400–6.
39 Niida Y, Stemmer-Rachamimov AO, Logrip M *et al.* Survey of somatic mutations in tuberous sclerosis complex (TSC) hamartomas suggests different genetic mechanisms for pathogenesis of TSC lesions. *Am J Hum Genet* 2001; **69**: 493–503.
40 Ingram DA, Yang FC, Travers JB *et al.* Genetic and biochemical evidence that haploinsufficiency of the *Nf1* tumor suppressor gene modulates melanocyte and mast cell fates *in vivo*. *J Exp Med* 2000; **191**: 181–8.
41 Cichowski K, Jacks T. *NF1* tumor suppressor gene function: narrowing the GAP. *Cell* 2001; **104**: 593–604.
42 Marsh DJ, Dahia PL, Coulon V *et al.* Allelic imbalance, including deletion of *PTEN/MMACI*, at the Cowden disease locus on 10q22-23, in hamartomas from patients with Cowden syndrome and germline *PTEN* mutation. *Genes Chromosomes Cancer* 1998; **21**: 61–9.
43 Venkatachalam S, Shi YP, Jones SN *et al.* Retention of wild-type *p53* in tumors from *p53* heterozygous mice: reduction of *p53* dosage can promote cancer formation. *EMBO J* 1998; **17**: 4657–67.

Antitumor activity of anti-C-ERC/mesothelin monoclonal antibody *in vivo*

Koichi Inami,[1,2] Masaaki Abe,[1] Kazuyoshi Takeda,[3] Yoshiaki Hagiwara,[1,4] Masahiro Maeda,[4] Tatsuya Segawa,[4] Masafumi Suyama,[2] Sumio Watanabe[2] and Okio Hino[1,5]

Departments of [1]Pathology and Oncology, [2]Gastroenterology and [3]Immunology, Juntendo University School of Medicine, Tokyo; [4]Immuno-Biological Laboratories Co., Ltd, Gunma, Japan

(Received June 15, 2009/Revised November 18, 2009/Accepted December 2, 2009)

Mesothelioma is an aggressive cancer often caused by chronic asbestos exposure, and its prognosis is very poor despite the therapies currently used. Due to the long latency period between asbestos exposure and tumor development, the worldwide incidence will increase substantially in the next decades. Thus, novel effective therapies are warranted to improve the prognosis. The ERC/mesothelin gene (*MSLN*) is expressed in wide variety of human cancers, including mesotheliomas, and encodes a precursor protein cleaved by proteases to generate C-ERC/mesothelin and N-ERC/mesothelin. In this study, we investigated the antitumor activity of C-ERC/mesothelin-specific mouse monoclonal antibody, 22A31, against tumors derived from a human mesothelioma cell line, ACC-MESO-4, in a xenograft experimental model using female BALB/c athymic nude mice. Treatment with 22A31 did not inhibit cell proliferation of ACC-MESO-4 *in vitro*; however, therapeutic treatment with 22A31 drastically inhibited tumor growth *in vivo*. 22A31 induced antibody-dependent cell-mediated cytotoxicity by natural killer (NK) cells, but not macrophages, *in vitro*. Consistently, the F(ab')^2 fragment of 22A31 did not inhibit tumor growth *in vivo*, nor did it induce antibody-dependent cell mediated cytotoxicity (ADCC) *in vitro*. Moreover, NK cell depletion diminished the antitumor effect of 22A31. Thus, 22A31 induced NK cell-mediated ADCC and exerted antitumor activity *in vivo*. 22A31 could have potential as a therapeutic tool to treat C-ERC/mesothelin-expressing cancers including mesothelioma. (*Cancer Sci* 2010)

Mesothelioma is an aggressive cancer stemming from transformation of mesothleial cells, which is usually associated with chronic asbestos exposure.[1] Due to the long latency period between asbestos exposure and tumor development, the worldwide incidence will increase substantially in the next decades.[2,3] The prognosis is very poor with a median survival of 4 to12 months despite the therapies currently used, including surgery, radiotherapy, and chemotherapy.[4,5] Because of the inefficacy of the conventional treatments, novel effective therapies are necessary for improving the prognosis of this devastating disease.

Erc was identified in renal cell cancers of the Eker rat, and is the homolog of human *MSLN*.[6,7] The ERC/mesothelin gene encodes a 71 kDa precursor protein, which is cleaved by proteases to yield 31-kDa N-terminal (N-ERC/mesothelin) and 40-kDa C-terminal (C-ERC/mesothelin) proteins.[8,9] N-ERC/mesothelin, originally identified as megakaryocyte-potentiating factor (MPF), is a soluble protein released into the extracellular space and is now used as a serum marker of mesothelioma.[10–21] C-ERC/mesothelin is a glycoprotein tethered to the cell surface by a glycosyl phosphatidyl inositol anchor, and it was reported that this protein promotes anchorage-independent growth and prevents anoikis.[8,9,22] C-ERC/mesothelin is expressed not only in normal mesothelial cells of the pleura, pericardium, and peritoneum, but also in malignant cells of mesotheliomas, pancreatic ductal carcinomas, ovarian cancers, and some other cancers.[8,23–26] Moreover, C-ERC/mesothelin is a possible target for immunotherapy because of its frequent expression.[9,27–34]

In this study, we investigated the antitumor activity of an anti-C-ERC/mesothelin monoclonal antibody (mAb) (22A31) that we have devised against tumors derived from a mesothelioma cell line.[35] Treatment with 22A31 itself did not affect tumor cell growth *in vitro*, but induce antibody-depend cell mediated cytotoxicity (ADCC) with natural killer (NK) cells, but not macrophages. 22A31 consistently exerted an antitumor effect *in vivo*, and which was not observed when the F(ab')^2 fragment of 22A31 was used or NK cells were depleted in mice. These results suggest that 22A31 is a possible therapeutic tool for C-ERC/mesothelin-expressing tumors including mesothelioma in clinical therapy.

Materials and Methods

Mice. Female BALB/c athymic nude (BALB/c nu/nu) mice at 7 weeks of age were purchased from Charles River Japan (Yokohama, Japan). Rag-2-deficient (RAG-2$^{-/-}$) C57BL/6 mice were derived as described previously.[36] All mice were maintained under specific pathogen-free conditions and all *in vivo* studies were approved by the Institute Animal Care and Use Committee of Juntendo University.

Cells and antibodies. ACC-MESO-4 cells, derived from human mesothelioma, were provided by RIKEN cell bank (Ibaraki, Japan), and cultured in RPMI-1640 medium supplemented with 10% fetal calf serum.[37] Huh7 cells, derived from human hepatocellular carcinoma, were purchased from RIKEN Cell Bank, and cultured in Dulbecco's Modified Eagle's Medium supplemented with 10% fetal calf serum. NCI-H226 cells, derived from human mesothelioma, were provided by the American Type Culture Collection (Manassas, VA, USA), and cultured in RPMI-1640 medium supplemented with 10% fetal calf serum. C-ERC/mesothelin-specific mouse monoclonal antibody, 22A31, was prepared in our laboratory as previously described.[35] Normal mouse IgG1κ was purchased from Sigma (St. Louis, MO, USA). F(ab')^2 fragment was prepared in our laboratory as previously described.[38] Generation of F(ab')^2-22A31 was confirmed by SDS-polyacrylamide gel electrophoresis (SDS-PAGE) using 10% Laemmli gel and Coomassie Brilliant Blue (CBB) staining.

Flow cytometric analysis. C-ERC/mesothlin expression on cell surface was analyzed by flow cytometry as previously described.[35] Briefly, 1×10^6 cells were incubated with 1 μg/mL of 22A31 or 1 μg/mL of normal mouse IgG1κ diluted in serum free medium (100 μL) at 4°C for 30 min. After washing with PBS, cells were resuspended in 100 μL of serum

[5]To whom correspondence should be addressed.
E-mail: ohino@juntendo.ac.jp

doi: 10.1111/j.1349-7006.2009.01463.x

free medium containing 2 μg/mL of Alexa Flour 488-conjugated goat antimouse IgG (Molecular Probes, Eugene, OR, USA) to detect the primary antibodies, and incubated at 4°C for 30 min. After washing with PBS, the stained cells were analyzed by a FACScan (BD Bioscience, San Jose, CA, USA).

Antitumor activity of 22A31 mAb in BALB/c nu/nu mice. To assess the antitumor activity of 22A31, 2×10^6 of tumor cells were inoculated subcutaneously into the right flank of BALB/c nu/nu mice. We commenced antibody treatments with 22A31 or isotype matched control IgG by intratumoral injection or intraperitoneal injection twice per week, when tumors become visible (4 mm × 4 mm, 16 mm^2). In some experiments, mice were treated with 200 μg of anti-asialo-GM1 Ab (Wako Pure Chemicals, Osaka, Japan) or control rabbit Ig every 4 days starting 2 days before 22A31 treatment. NK cell depletion was confirmed by flow cytometric analysis in anti-asialo GM1 Ab-treated mice. Tumor bearing-mice were monitored for tumor development and progression. Tumor size was determined by caliper measurement of the largest (a) and smallest perpendicular diameters (b) and height (c), and was calculated using following the formula: Volume = 4 π $a \times b \times c/3$. After the completion of the experiment, mice were euthanized.

Immunohistochemistry. Three-cm thick tissue sections were prepared from archival formalin-fixed, paraffin-embedded specimens. After deparaffinization, the tissue sections were heated in 10 mM citrate buffer (pH6) for antigen retrieval and then treated with 3% hydrogen peroxide. Then, the sections were incubated with antibody solutions diluted in Tris-buffered saline with

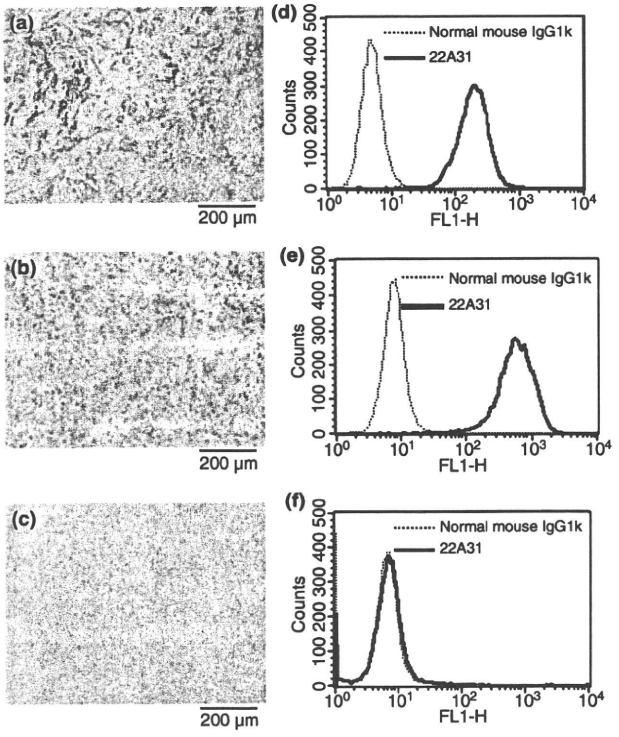

Fig. 1. Expression of C-ERC/mesothelin in ACC-MESO-4, NCI-H226, and Huh7 cells. Immunohistochemical localization of C-ERC/mesothelin in ACC-MESO-4 cell- (a), NCI-H226 cell- (b), and Huh7 cell- (c) derived xenografts. Indicated panel is representative of xenograft specimens. Original magnification, ×100. Surface expression of C-ERC/mesothelin on ACC-MESO-4 cells (d), NCI-H226 cells (e), and Huh7 cells (f) analyzed by flow cytometry. Solid line denotes staining of 22A31 and detected with Alexa Flour-488. Dashed line denotes staining normal mouse IgG1κ.

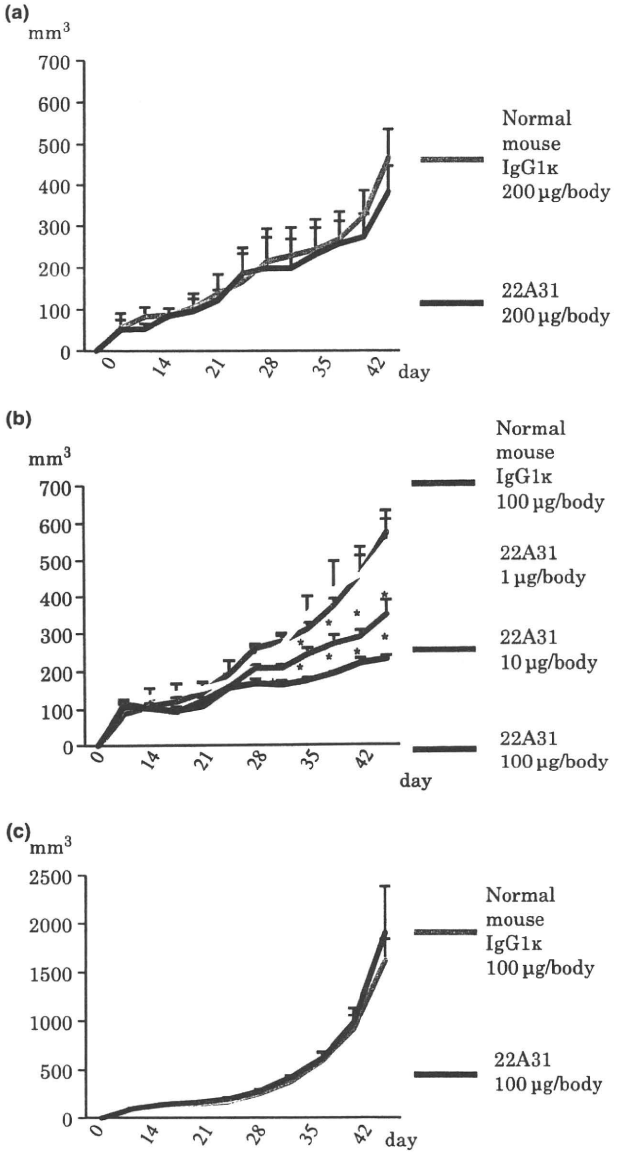

Fig. 2. *In vivo* antitumor activity of 22A31. (a) Antitumor effect of 22A31 intraperitoneal injection against ACC-MESO-4 tumor cell. (b) Antitumor effect of 22A31 intratumoral injection against ACC-MESO-4 tumor cells. (c) Antitumor effect of 22A31 intratumoral injection against C-ERC/mesothelin-negative Huh7 tumor cells. 22A31 or normal mouse IgG1κ (control Ab) was given twice per week. Mice were treated 10 times with the respective antibody. Median tumor volume and SD of xenografts are indicated (n = 3–5). Asterisk mark indicates statistical significance.

0.1% Tween 20 overnight at 4°C. We used biotin-conjugated 22A31 (1:300 dilution) as the primary antibody. Diaminobenzidine was used as the substrate for peroxidase. DX50F-3, DP-25, and DP2-BSW (Olympus. Tokyo, Japan) were used for the acquisition of images.

Cell proliferation assay. Tumor cells grown under regular culture condition were harvested and resuspended in RPMI-1640 medium at a concentration 8×10^4 cells/mL. Twenty-five μL of cell suspensions and 25 μL of antibody solutions were added to 96-well plates. After 72 h of incubation at 37°C with 5% CO2 atmosphere, XTT assay was performed using

doi: 10.1111/j.1349-7006.2009.01463.x

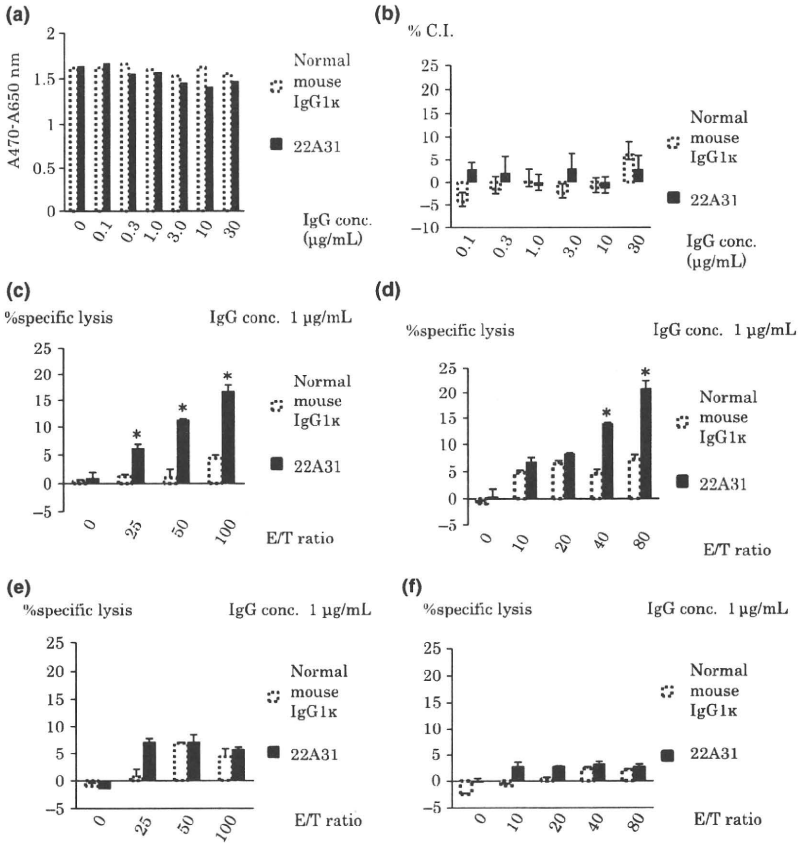

Fig. 3. *In vitro* antitumor activity of 22A31. (a) Direct effect of 22A31 on ACC-MESO-4 tumor cell growth. After 72 h of incubation with indicated concentration of 22A31 (black bar) or normal mouse IgG1k (white bar), XTT assay was performed and absorbance was presented. (b) 22A31-induced complement-dependent cytotoxicity (CDC). %Cytotoxicity index (C.I.) of the indicated concentrations of 22A31 or normal mouse IgG1k against ACC-MES-4 tumor cells are indicated. (c,d) 22A31-inducd antibody-dependent cell mediated cytotoxicity (ADCC) against ACC-MESO-4 tumor cells (c) or NCI-H226 tumor cells (d) with purified natural killer (NK) cells. ADCC induced by 1 μg/mL of 33A31 or normal mouse IgG1κ was examined at indicated effector/target ratios when purified NK cells were used as effector cells. (e) 22A31-inducd ADCC against C-ERC/mesothelin-negative Huh7 tumor cells with purified NK cells. ADCC induced by 1 μg/mL of 33A31 or normal mouse IgG1κ was examined at indicated effector/target ratios when purified NK cells were used as effector cells. (f) 22A31-inducd ADCC against ACC-MESO-4 tumor cells with purified macrophages. ADCC induced by 1 μg/mL of 33A31 or normal mouse IgG1κ was examined at indicated effector/target ratios when purified macrophages were used as effector cells. Asterisk indicates statistical significance.

50 μL of XTT mixture containing 200 μL/mL of XTT and 25 μM of menatione (Roche Diagnostics, Mannheim, Germany) for 4 h. Absorbance at 470–650 nm was measured in an ELISA reader (E-MAX; Molecular Devices, Sunnyvale, CA, USA).

Antibody-dependent cell mediated cytotoxicity (ADCC) assay. Cytotoxic activity was tested by a 4-h ^{51}Cr release assay as previously described.[36] Freshly isolated splenic and peritoneal mononuclear cells derived from B6 RAG-$2^{-/-}$ mice were stained with phycoerythrin (PE)-conjugated anti-DX5 mAb (eBioscience, San Diego, CA, USA) or PE-conjugated anti-CD14 mAb (eBioscience), and $DX5^+$ NK cells or $CD14^+$ macrophages were enriched by auto MACS using PE microbeads (Miltenyi Biotec, Bergisch Glabach, Germany), respectively, according to the manufacturer's instructions. These purified cells were subsequently used as the effector cells in the ADCC assay.

Complement-dependent cytotoxicity (CDC) assay. Complement-mediated lysis with rabbit serum (Low-Tox M; Cedarlane Laboratories, Hornby, ON, Canada) was performed as previously described.[39] After incubation, cellular viability was determined by Trypan blue exclusion. Cytotoxicity index (C.I.) was calculated using the following formula: % C.I. = (sample % cell death − control % cell death)/(100 − control % cell death) × 100%.

Statistical analysis. We analyzed the data of xenografts treated with antibodies, using JMP and SAS version 8.1.3 (SAS Institute, Cary, CA, USA). To compare the volume of tumors between groups, the Mann–Whitney *U*-test was useed. The two-sample *t*-test was used for cell proliferation, and the ADCC and CDC assays. $P < 0.05$ was considered statistically significant.

Results

C-ERC/mesothelin expression in target cells. Cell surface expression of C-ERC/mesothelin on ACC-MESO-4 tumor cells and NCI-H226 tumor cells, but not Huh7 tumor cells, was demonstrated by both flow cytometric and immunohistochemical analysis (Fig. 1). Thus, ACC-MESO-4 and NCI-H226 tumor cells constitutively expressed C-ERC/mesothelin even after xenograft transplantation into nude mice.

Antitumor activity of 22A31 in mice xenograft model. When 22A31 was intraperitonealy injected into ACC-MESO-4 tumor-bearing mice, 22A31 did not significantly inhibit tumor growth compared with normal mouse IgG1κ (Fig. 2a). However, intratumoral injection of 22A31 significantly inhibited the growth of ACC-MESO-4 tumors, but not Huh7 tumors, compared with normal mouse IgG1κ (Fig. 2b,c). Moreover, this antitumor effect of 22A31 was demonstrated to occur in a dose-dependent manner (Fig. 2b). These results suggest that 22A31 exerts an antitumor effect against C-ERC/mesothelin-expressing tumor cells *in vivo* when administrated intratumorally.

22A31 triggered ADCC *in vitro*. Then, we examined the possible mechanisms involved in the 22A31-induced antitumor effect *in vitro*. The cell proliferation assay using XTT did not show a direct inhibitory effect of 22A31 on the growth of ACC-MESO-4 tumor cells *in vitro* (Fig. 3a). Furthermore, 22A31 did not induce CDC against ACC-MESO-4 cells (Fig. 3b). However, 22A31 induced ADCC when ACC-MESO-4 cells were incubated with purified NK cells, and that was in an effector/target ratio-dependent manner (Fig. 3c). 22A31 also induced ADCC against C-ERC/mesothlelin-expressing NCI-H226 cells, but not Huh7 cells, which did not express C-ERC/mesothelin when incubated with purified NK cells (Fig. 3d,e), although both cells

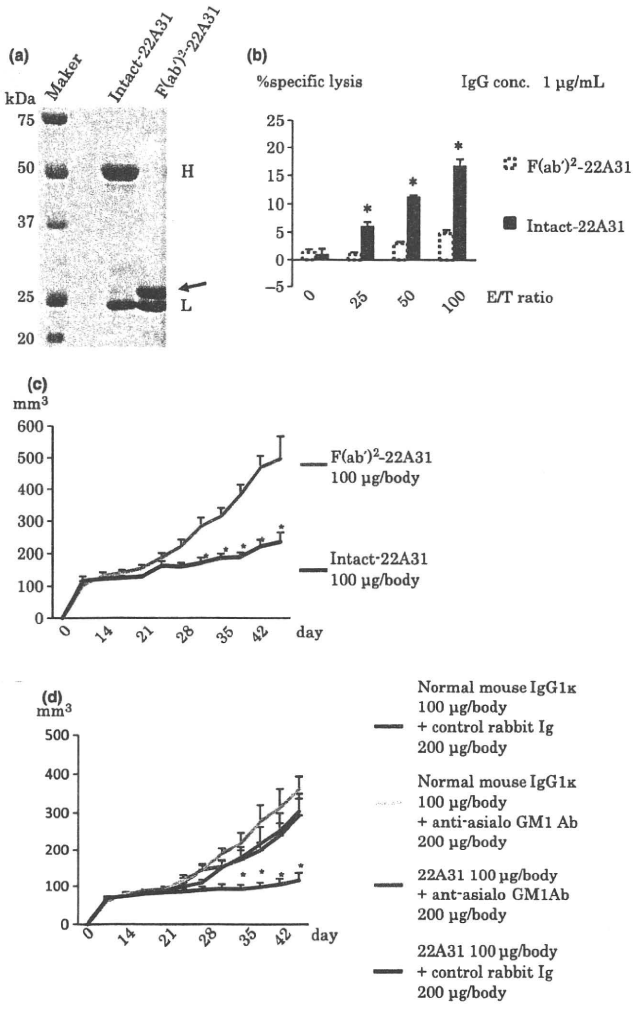

Fig. 4. Contribution of the Fc portion and natural killer (NK) cells to the antitumor effect of 22A31 *in vivo*. (a) Preparation of 22A31 $F(ab')^2$ fragment. Ten μg of intact-22A31 or $F(ab')^2$-22A31 were electrophoresed using SDS-PAGE and visualized Coomassie Brilliant Blue (CBB)-staining. Arrow indicates heavy chain of $F(ab')^{22}$-22A31. H and L indicate heavy chain of intact-22A31 and light chain of both antibodies. (b) Intact- or $F(ab')^2$-22A31-inducd ADCC against ACC-MESO-4 tumor cells with purified NK cells. ADCC induced by 1 μg/mL of Intact- or $F(ab')^2$-22A31 was examined at indicated effector/target ratios when purified NK cells were used as effector cells. (c) Antitumor effect of intact- or $F(ab')^2$-22A31 against ACC-MESO-4. One hundred μg/body of Intact-22A31 or $F(ab')^2$-22A31 was intratumorally injected twice per week. Mice were treated 10 times with the respective antibody. Median tumor volume and SD of xenografts are indicated (n = 5). (d) Antitumor effect of 22A31 in NK cell-depleted mice. ACC-MESO-4 tumor-bearing mice were treated with 200 μg/body of anti-asialo GM1 Ab to deplete NK cells or control rabbit Ig, then intratumorally injected with 100 μg/body of intact-22A31 or control Ig twice per week as described in the Materials and Methods. Median tumor volume and SD of xenografts are indicated (n = 5). Asterisk indicates statistical significance.

might be sensitive to direct NK-mediated cytotoxicity. Besides, 22A31 did not induce ADCC against C-ERC/mesothelin-expressing ACC-MESO-4 when incubated with purified macrophages (Fig. 3f).

Critical contribution of Fc portion and NK cells to antitumor effect of 22A31 *in vivo*. The Fc portion of antibodies, which binds to the Fc receptor on NK cells and complement, is critical for ADCC induction.[40] Thus, we examined the antitumor effect of 22A31 $F(ab')^2$ fragment (Fig. 4a). The $F(ab')^2$ fragment of 22A31 did not induce ADCC *in vitro* (Fig. 4b), and administration of 22A31 $F(ab')^2$ fragment consistently did not inhibit the growth of ACC-MESO-4 tumor compared with intact 22A31 *in vivo* (Fig. 4c). Moreover, the antitumor effect of 22A31 was inhibited when NK cells were depleted in mice by anti-asialo-GM1 Ab treatment (Fig. 4d). Taken together, these results suggested that 22A31 exerts antitumor effect against C-ERC/mesothelin-expressing tumor cells via NK cell-mediated ADCC *in vivo*.

Discussion

C-ERC/mesothelin is expressed in various human cancer cells, particularly in malignant mesothelioma, which has poor prognosis.[4,5] C-ERC/mesothelin is believed to be a possible target for immunotherapy against these cancers; thus we here examined the therapeutic antitumor effect of anti-C-ERC/mesothelin monoclonal antibody, 22A31, which we had previously developed.[35]

In a xenograft model using BALB/c nu/nu mice, intratumoral administration of 22A31 inhibited the growth of C-ERC/mesothelin-expressing ACC-MESO-4 tumor cells in a dose-dependent manner, but not the growth of C-ERC/mesothelin-negative Huh-7 tumor cells. 22A31 induced ADCC against C-ERC/mesothelin-expressing ACC-MESO-4 cells and NCI-H226 cells, but not Huh7 tumor cells, and this 22A31-mediaed ADCC was observed with incubation with purified NK cells, but not purified macrophages. Moreover, the antitumor effect of 22A31 was inhibited when the mice were treated with the $F(ab')^2$ fragment of 22A31 or NK cells were depleted during the treatment with intact 22A31. Thus, 22A31 effected NK cell-mediated ADCC which resulted in an antitumor effect against C-ERC/mesothelin-expressing human cancers *in vivo*, indicating the possible utility of 22A31 in clinical therapy.

It was reported that C-ERC/mesothelin promotes anchorage-independent growth and prevents anoikis.[22] However, there are no anatomical and historical abnormalities in C-ERC/mesothelin knockout mice, and physiological and pathogenic functions of C-ERC/mesothelin have not been fully revealed.[41] We did not observe any inhibitory effect of 22A31 on the proliferation of some C-ERC/mesothelin-expressing tumor cells including ACC-MESO-4 tumor cells *in vitro*. Moreover, we did not detect any 22A31-induced apoptosis or autophagic cell death by caspase-3/7 activity assay or LC-3 immunoblotting analysis. These results indicate that 22A31 does not inhibit tumor growth directly. Further studies are needed to clarify the roles of C-ERC/mesothelin in tumor cells, which will provide critical information for improving the antitumor effect of anti-C-ERC/mesothelin mAb.

It is now commonly accepted that tumor-targeting mAbs, such as anti-HER2/neu/ErbB-2 mAb and anti-epidermal growth factor mAb, demonstrate significant therapeutic effects in cancer patients.[42] Direct antitumor effect by tumor-targeting mAbs is possibly involved; however, multiple mechanisms, including ADCC and CDC, have been reported to generally contribute to the antitumor effect of tumor-targeting mAbs.[43] Moreover, it was reported that induction of tumor antigen-specific cytotoxic T cells (CTL) is critical for successful antibody-based tumor-targeting therapy.[44,45] Thus, 22A31 treatment possibly induced ACC-MESO-4 tumor-specific CTL during the therapy; however, we could not examine this possibility because we used a xenograft experimental model featuring athymic nude mice. Further basic studies using humanized mice, such as NOD/Shi-scid/IL-2 receptor γ null (NOG) mice with humanized 22A31, are needed to reveal the complete mechanisms of the antitumor effect of 22A31 *in vivo*.[46]

doi: 10.1111/j.1349-7006.2009.01463.x

C-ERC/mesothelin is expressed not only in mesotheliomas, but also in pancreatic ductal carcinomas, ovarian cancers, and some other cancers.[8,23–26] Pancreatic ductal carcinoma is also a particularly devastating disease because of its poor prognosis. The overall 5-year survival rate of these patients is under 10%.[47,48] Early diagnosis of ovarian cancers is so difficult that the 5-year survival is only 35–40%.[49] Novel therapic strategies against C-ERC/mesothelin-expressing tumors, including mesothelioma, pancreatic cancer, and ovarian cancer, are warranted. The results presented here suggest the possible utility of 22A31 to treat cancers; however, intraperitoneal administration of 22A31 did not significantly exert antitumor effect, possibly due to insufficient intratumor concentration of 22A31. Thus, further studies are needed to advance drug delivery within the tumor mass to augment the therapeutic effect of 22A31. We are now going to humanize 22A31 with the hope that this may improve the prognosis of patients with C-ERC/mesothelin-expressing tumors.

Acknowledgments

We would like to thank Masumi Maruo, Hidehiro Okura, Sun Guo Dong, Wang Lu, Piao Xiang Hua, Kazu Shiomi, Danqing Zhang, Shuji Matsuoka, Toshiyuki Kobayashi, and members of the Department of Gastroenterology, Juntendo Hospital, for their help in the preparation of this study. This work was supported by a Grant-in-Aid for Cancer Research and Grants-in-Aid for Scientific Research from the Ministry of Education, Culture, Sports and Science and Technology of Japan and the Ministry of Health, Labor and Welfare of Japan. This study was partially supported by a consignment expense for the molecular imaging program on 'Research Base for PET Diagnosis' from the Ministry of Education, Culture, Sport, and Science and Technology, Government of Japan.

References

1 Britton M. The epidemiology of mesothelioma. *Semin Surg Oncol* 2002; **29**: 18–25.
2 Connelly RR, Spirtas R, Myers MH, Percy CL, Fraumeni JF Jr. Demographic patterns for mesothelioma in the United States. *J Natl Cancer Inst* 1987; **78**: 1053–60.
3 Ismaril-Khan R, Robinson LA, Williams CC Jr, Garrett CR, Bepler G, Simon GR. Malignant pleural mesothelioma, a comprehensive review. *Cancer Control* 2006; **13**: 255–63.
4 Pass H. Malignant pleural mesothelioma, surgical roles and novel therapies. *Clin Lung Cancer* 2001; **3**: 102–17.
5 Kanazawa N, Ioka A, Tsukuma H, Ajiki W, Oshima A. Incidence and survival of mesothelioma in Osaka, Japan. *Jpn J Clin Oncol* 2006; **36**: 254–7.
6 Hino O, Kobayashi E, Nishizawa M *et al.* Renal carcinogenesis in the Eker rat. *J Cancer Res Clin Oncol* 1995; **121**: 602–5.
7 Yamashita Y, Yokoyama M, Kobayashi E, Takai S, Hino O. Mapping and determination of the cDNA sequence of the Erc gene preferentially expressed in renal cell carcinoma in the Tsc2 gene mutant (Eker) rat model. *Biochem Biophys Res Commun* 2000; **275**: 134–40.
8 Chang K, Pastan I. Molecular cloning of mesothelin, a differentiation antigen present on mesothelium, mesotheliomas, and ovarian cancers. *Proc Natl Acad Sci USA* 1996; **93**: 136–40.
9 Raffit H, Tapan B, Ira P. Mesothelin: a new target for immunotherapy. *Clin Cancer Res* 2004; **10**: 3937–42.
10 Yamaguchi N, Hattori K, Oh-eda M, Kojima T, Imai N, Ochi N. A novel cytokine exhibiting megakaryocyte potentiating activity from a human pancreatic tumor cell line HPC-Y5. *J Biol Chem* 1994; **269**: 805–8.
11 Kojima T, Oh-eda M, Hattori K *et al.* Molecular cloning and expression of megakaryocyte potentiating factor cDNA. *J Biol Chem* 1995; **270**: 21984–90.
12 Maeda M, Hino O. Molecular tumor marker for asbestos-related mesothelioma: serum diagnostic markers. *Pathol Int* 2006; **56**: 649–54.
13 Maeda M, Hino O. Blood test for asbestos-related mesothelioma. *Oncology* 2006; **71**: 26–31.
14 Shiomi K, Miyamoto H, Segawa T *et al.* Novel ELISA system for detection of N-ERC/mesothelin in the sera of mesothelioma patients. *Cancer Sci* 2006; **97**: 928–32.
15 Shiomi K, Hagiwara Y, Sonoue K *et al.* Sensitive and specific new enzyme-linked immunosorbent assay for N-ERC/meosthelin increases its potential as a useful serum tumor marker for mesothelioma. *Clin Cancer Res* 2008; **14**: 1431–7.
16 Hino O, Shiomi K. Diagnostic biomarker of asbestos-related mesothelioma: example of translational research. *Cancer Sci* 2007; **98**: 1147–57.
17 Scholler N, Fu N, Yang Y *et al.* Soluble member(s) of the mesothelin/megakaryocyte potentiating factor family are detectable in sera from patients with ovarian carcinoma. *Proc Natl Acad Sci USA* 1999; **96**: 11531–6.
18 Onda M, Nagata S, Ho M *et al.* Megakaryocyte potentiation factor cleaved from mesothelin precursor is a useful tumor marker in the serum of patients with mesothelioma. *Clin Cancer Res* 2006; **12**: 4225–31.
19 Hassan R, Remaley AT, Sampson ML *et al.* Detection and quantitation of serum mesothelin, a tumor marker for patients with mesothelioma and ovarian cancer. *Clin Cancer Res* 2006; **12**: 447–53.
20 Robinson BW, Creaney J, Lake R *et al.* Mesothelin-family proteins and diagnosis of mesothelioma. *Lancet* 2003; **15**: 1612–6.
21 Robinson BW, Creaney J, Lake R *et al.* Soluble mesothelin-related protein – a blood test for mesothelioma. *Lung Cancer* 2005; **49**: S109–11.
22 Uehara N, Matshoka Y, Tsubura A. Mesothelin promotes anchorage-independent growth and prevents anoikis via extracellular signal-regulated kinase signaling pathway in human breast cancer cells. *Mol Cancer Res* 2008; **6**: 186–93.
23 Argani P, Iacobuzio-Donahue C, Ryu B *et al.* Mesothelin is overexpressed in the vast majority of ductal adenocarinomas of the pancreas: identification of a new pancreatic cancer marker by serial analysis of gene expression (SAGE). *Clin Cancer Res* 2001; **7**: 3862–8.
24 Baruch AC, Wang H, Staerkel GA, Evans DB, Hwang RF, Krishnamurthy S. Immunocytochemical study of the expression of mesothelin in fine-needle aspiration biopsy specimens of pancreatic adenocarcinoma. *Diagn Cytopathol* 2007; **35**: 143–7.
25 Yaziji H, Battifora H, Barry TS *et al.* Evaluation of 12 antibodies for distinguishing epithelioid mesothelioma from adenocarcinoma: identification of a three-antibody immunohistochemical panel with maximal sensitivity and specificity. *Mod Pathol* 2006; **19**: 514–23.
26 Inami K, Kajino K, Abe M *et al.* Secretion of N-ERC/mesothelin and expression of C-ERC/mesothelin in human pancreatic ductal carcinoma. *Oncol Rep* 2008; **20**: 1375–80.
27 Li M, Bharadwaj U, Zhang R *et al.* Mesothelin is a malignant factor and therapeutic vaccine target for pancreatic cancer. *Mol Cancer Ther* 2008; **7**: 286–96.
28 Hung CF, Tsai YC, He L, Wu TC. Control of mesothelin-expressing ovarian cancer using adoptive transfer of mesothelin peptide-specific CD8 + T cells. *Gene Ther* 2007; **14**: 921–9.
29 Hassan R, Btoaddus VC, Wilson S, Liewehr DJ, Zhang J. Anti-mesothelin immunotoxin SS1P in combination with gemcitabine results in increased activity against mesothelin-expressing tumor xenografts. *Clin Cancer Res* 2007; **13**: 7166–71.
30 Hassan R, Ebel W, Routhier EL *et al.* Preclinical evaluation of MORAb-009, a chimeric antibody targeting tumor-associated mesothelin. *Cancer Immun* 2007; **7**: 20.
31 Hassan R, Bullock S, Premkumar A *et al.* Phase I study of SS1P, a recombinant anti-mesothelin immunotoxin given as a bolus I.V. infusion to patients with mesothelin-expressing mesothelioma, ovarian, and pancreatic cancers. *Clin Cancer Res* 2007; **13**: 5144–9.
32 Hassan R, Williams-Gould J, Steinberg SM *et al.* Tumor-directed radiation and the immunotoxin SS1P in the treatment of mesothelin-expressing tumor xenografts. *Clin Cancer Res* 2006; **12**: 4983–8.
33 Sato N, Hassan R, Axworthy DB *et al.* Pretargeted radioimmunotherapy of mesothelin-expressing cancer using a tetravalent single-chain Fv-streptavidin fusion protein. *J Nucl Med* 2005; **46**: 1201–9.
34 Thomas AM, Santarsiero LM, Lutz ER *et al.* Mesothelin-specific CD8 (+) T cell responses provide evidence of in vivo cross-priming by antigen-presenting cells in vaccinated pancreatic cancer patients. *J Exp Med* 2004; **200**: 297–306.
35 Ishikawa K, Segawa T, Hagiwara Y, Maeda M, Abe M, Hino O. Establishment of novel monoclonal antibody to human ERC/mesothelin useful for study and diagnosis of ERC/mesothelin-expressing cancers. *Pathol Int* 2009; **59**: 161–6.
36 Takeda K, Hayakawa Y, Smyth MJ *et al.* Involvement of tumor necrosis factor-related apoptosis-inducing ligand in surveillance of tumor metastasis by liver natural killer cells. *Nat Med* 2001; **7**: 94–100.
37 Usami N, Fukui T, Kondo M *et al.* Establishment and characterization of four malignant pleural mesothelioma cell lines from Japanese patients. *Cancer Sci* 2006; **97**: 387–94.
38 Wilson DS, Wu J, Peluso P, Nock S. Improved method for pepsinolysis of mouse IgG(1) molecules to $F(ab')^2$(2) fragments. *J Immunol Methods* 2002; **260**: 29–36.

39 Takeda K, Dennert G. The development of autoimmunity in C57BL/6 lpr mice correlates with the disappearance of natural killer type 1-positive cells: evidence for their suppressive action on bone marrow stem cell proliferation, B cell immunoglobulin secretion, and autoimmune symptoms. *J Exp Med* 1993; **177**: 155–64.
40 Rouard H, Tamasdan S, Moncuit J *et al.* Fc receptors as targets for immunotherapy. *Int Rev Immunol* 1997; **16**: 147–85.
41 Bera TK, Pastan I. Mesothelin is not required for normal mouse development or reproduction. *Mol Cell Biol* 2000; **20**: 2902–6.
42 Pegram MD, Lipton A, Hayes DF *et al.* Phase II study of receptor-enhanced chemosensitivity using recombinant humanized anti-p185HER2/neu monoclonal antibody plus cisplatin in patients with HER2/neu-overexpressing metastatic breast cancer refractory to chemotherapy treatment. *J Clin Oncol* 1998; **16**: 2659–71.
43 Takeda K, Okumura K, Smyth MJ. Combination antibody-based cancer immunotherapy. *Cancer Sci* 2007; **98**: 1297–302.
44 zum Büschenfelde CM, Hermann C, Schmidt B, Peschel C, Bernhard H. Antihuman epidermal growth factor receptor 2 (HER2) monoclonal antibody trastuzumab enhances cytolytic activity of class I-restricted HER2-specific T lymphocytes against HER2-overexpressing tumor cells. *Cancer Res* 2002; **62**: 2244–7.
45 Dhodapkar KM, Krasovsky J, Williamson B, Dhodapkar MV. Antitumor monoclonal antibodies enhance cross-presentation of cellular antigens and the generation of myeloma-specific killer T cells by dendritic cells. *J Exp Med* 2002; **195**: 125–33.
46 Ito M, Kobayashi K, Nakahata T. NOD/Shi-scid IL2rgamma(null) (NOG) mice more appropriate for humanized mouse models. *Curr Top Microbiol Immunol* 2008; **324**: 53–76.
47 Wray CJ, Ahmad SA, Matthews JB, Lowy AM. Surgery for pancreatic cancer: recent controversies and current practice. *Gastroenterology* 2005; **128**: 1626–41.
48 Li D, Xie K, Wolff R, Abbruzzese JL. Pancreatic cancer. *Lancet* 2004; **363**: 1049–57.
49 Singh AP, Senapati S, Ponnusamy MP *et al.* Clinical potential of mucins in diagnosis, prognosis, and therapy of ovarian cancer. *Lancet Oncol* 2008; **9**: 1076–85.

doi: 10.1111/j.1349-7006.2009.01463.x

Original article

Nuclear Medicine Communications

Development of positron emission tomography imaging by ^{64}Cu-labeled Fab for detecting ERC/mesothelin in a mesothelioma mouse model

Chisato Yoshida[a,c], Chizuru Sogawa[a], Atsushi B. Tsuji[a], Hitomi Sudo[a,d], Aya Sugyo[a], Tomoya Uehara[c], Okio Hino[d], Yukie Yoshii[e], Yasuhisa Fujibayashi[e], Toshimitsu Fukumura[b], Mitsuru Koizumi[a], Yasushi Arano[c] and Tsuneo Saga[a]

Background **Malignant mesothelioma is a highly aggressive form of cancer. Curative surgery is the only effective therapy for mesothelioma, and therefore early diagnosis is important. However, early diagnosis is difficult using current diagnostic imaging techniques, and a new imaging method for early diagnosis is urgently required. We evaluated the affinity of radiolabeled monoclonal antibodies to the C-terminal fragment of ERC/mesothelin for this purpose.**

Methods **^{111}In-labeled or ^{125}I-labeled IgG against C-terminal fragment of ERC and its Fab fragment were evaluated *in vitro* by cell binding, competitive inhibition, and cellular internalization assays, and *in vivo* by biodistribution in mice bearing ERC-expressing tumors. Next, the Fab fragment was labeled with the positron emitter ^{64}Cu and evaluated by positron emission tomography (PET).**

Results **Radiolabeled IgG and Fab showed specific binding to ERC-expressing mesothelioma cells with high affinity. Both radiolabeled IgG and Fab internalized into cells after binding to ERC on the cell surface. ^{111}In-labeled IgG accumulated in ERC-expressing tumors and resulted in a moderate tumor-to-blood ratio at 4 days after injection. Furthermore, PET using ^{64}Cu-labeled Fab visualized the tumor at 6 h after injection.**

Conclusion **^{64}Cu-labeled Fab can be useful for ERC-specific PET imaging, and can thus facilitate improved diagnosis of patients with early-stage mesothelioma. *Nucl Med Commun* 00:000–000 © 2010 Wolters Kluwer Health | Lippincott Williams & Wilkins.**

Nuclear Medicine Communications 2010, 00:000–000

Keywords: antibody, ERC/mesothelin, mesothelioma, positron emission tomography

[a]Diagnostic Imaging Group, [b]Molecular Probe Group, Molecular Imaging Center, National Institute of Radiological Sciences, Anagawa, Inage-ku, [c]Department of Molecular Imaging and Radiotherapy, Graduate School of Pharmaceutical Sciences, Chiba University, Inohana, Chuo-ku, Chiba, [d]Department of Pathology and Oncology, Juntendo University School of Medicine, Hongo, Bunkyo-ku, Tokyo and [e]Biomedical Imaging Research Center, University of Fukui, Yoshida, Fukui, Japan

Correspondence to Dr Atsushi B. Tsuji, PhD, Diagnostic Imaging Group, Molecular Imaging Center, National Institute of Radiological Sciences, 4-9-1 Anagawa, Inage-ku, Chiba 263-8555, Japan
Tel: +81 43 206 4643; fax: +81 43 206 4138; e-mail: a_tsuji@nirs.go.jp

Chisato Yoshida and Chizuru Sogawa contributed equally to this study

Received 25 September 2009 **Revised** 1 December 2009
Accepted 10 December 2009

Introduction

Malignant mesothelioma is a highly aggressive form of cancer arising from the serosal surfaces of the pleura, peritoneum, and pericardium [1,2]. Approximately 75% of all cases involve the pleura, whereas the remaining 25% involve the peritoneum or pericardium. Mesothelioma is associated with past asbestos exposure, and has a latency of 30–40 years. The three major subtypes of mesothelioma are epithelioid (50–70% of all cases), sarcomatoid (7–20%), and mixed/biphasic (20–30%). This type of tumor was once rare, but the incidence is expected to increase worldwide over the next several decades as a result of widespread asbestos exposure, both occupational and environmental, in many countries [1–4].

Current treatment includes some form of surgery, which may be combined with chemotherapy and/or radiation. However, the prognosis of patients with this multimodality therapy remains poor [1,2]. Survival depends on stage, histological subtype, patient age, sex, and various other factors. Sugarbaker *et al.* [5] reported median survival rates of 25, 20, and 16 months for patients with stage I, II, and III of the disease, respectively. This finding indicates that early diagnosis is important in improving prognosis. However, early diagnosis is difficult using current diagnostic imaging techniques. The development of a new imaging method for the early diagnosis of mesothelioma is urgently required.

ERC/mesothelin is a 71 kDa cell surface antigen and is present on mesothelium, mesotheliomas, and ovarian cancers. This protein is physiologically cleaved by furin-like proteases into a 40 kDa C-terminal fragment (C-ERC) that remains membrane-bound and a 31 kDa N-terminal fragment (N-ERC) that is secreted into the bloodstream [6]. Recently, we developed new monoclonal antibodies against C-ERCs and N-ERCs [6,7] and reported that serum levels of N-ERC of patients with

0143-3636 © 2010 Wolters Kluwer Health | Lippincott Williams & Wilkins

DOI: 10.1097/MNM.0b013e328336733d

epithelioid mesothelioma were higher than those with other diseases [8]. A sensitive serum N-ERC assay applied in a population with a history of asbestos exposure is expected to detect patients with early-stage disease. Image-guided biopsy of such patients is thought to facilitate definitive diagnosis at early stages of disease. This is carried out using a noninvasive imaging method for detecting C-ERC, in which radiolabeled antibody is expected to play an important role. Although antibodies against C-ERC, ^{111}In-labeled IgG [9] and ^{111}In-labeled tetravalent scFv [10], have previously been evaluated by other research groups, the major aim of such studies was the development of therapeutic agents. Consequently, the same research groups have recently conducted clinical trials for the treatment of ERC-expressing tumors [11]. Positron emission tomography (PET), with higher sensitivity and greater quantification ability than single-photon emission computed tomography, seems to be suitable for the detection of ERC expression in early-stage mesothelioma.

In this study, we performed in-vitro and in-vivo investigations of ^{111}In-labeled or ^{125}I-labeled anti-C-ERC IgG and its Fab fragment to evaluate their use as an imaging probe for detecting ERC expression. To apply this Fab fragment to PET imaging, we labeled Fab with positron-emitting ^{64}Cu and monitored in-vivo distribution through PET imaging of human mesothelioma xenografts in nude mice.

Methods

Cell culture

Human mesothelioma cell lines, H226 and 211H, were obtained from American Type Culture Collection (Manassas, Virginia, USA). These cell lines were maintained in RPMI1640 (Sigma, St Louis, Missouri, USA) containing 5% fetal bovine serum in a humidified incubator maintained at 37°C with 5% CO_2. ERC was highly expressed in H226 cells and slightly in 211H cells [12].

Chelate conjugation and radiolabeling with ^{111}In, ^{125}I, and ^{64}Cu

Anti-C-ERC mouse monoclonal IgG_{2a} (22A31) [7] and its Fab fragment were conjugated with *N*-[(*R*)-2-amino-3-(*p*-isothiocyanato-phenyl)propyl]-*trans*-(*S*,*S*)-cyclohexane-1,2-diamine-*N*,*N*,*N*′,*N*″,*N*‴-penta-acetic acid [*p*-SCN-Bz-CHX-A″-DTPA (DTPA), Macrocyclics, Dallas, Texas, USA] or 2-(4-isothiocyanatobenzyl)-1,4,7,10-tetra-azacyclododecane-1,4,7,10-tetra-acetic acid [*p*-SCN-Bz-DOTA (DOTA), Macrocyclics]. Either the IgG or Fab antibody was incubated with DTPA or DOTA in 0.05 mol/l borate buffer (pH 8.5) for 16 h at 37°C. The conjugation ratio of DTPA and DOTA to antibody was estimated to be 1.7–2.1. ^{111}In chloride (Nihon Medi-Physics, Tokyo, Japan) prepared in 1 mol/l of acetate buffer (pH 6.0) was incubated with the DTPA-conjugated or DOTA-conjugated antibody for 30 min at room temperature or 37°C, respectively. The labeling efficiency of ^{111}In-labeled or ^{125}I-labeled antibodies was determined by cellulose acetate electrophoresis. The radiolabeled antibodies were purified by a Sephadex G-50 (GE Healthcare, Little Chalfont, UK) column. The specific activity of ^{111}In-DTPA-IgG and ^{111}In-DTPA-Fab was approximately 50 and 55 kBq/μg, respectively. ^{64}Cu chloride was produced by a cyclotron in our institute according to a previously reported method [13]. The DOTA-conjugated Fab was incubated with 37 MBq of ^{64}Cu in 0.1 mol/l ammonium citrate (pH 5.5) for 1 h at 37°C. The ^{64}Cu-DOTA-Fab was purified by a Sephadex G-50 column. Labeling efficiency was determined by thin-layer chromatography using 80% methanol as the mobile phase, and the radiolabeled antibodies were purified by a Sephadex G-50. The specific activity of ^{64}Cu-DOTA-Fab was 74–140 kBq/μg. Radioiodination was performed using the chloramine-T method [14]. The specific activity of ^{125}I-IgG and ^{125}I-Fab was approximately 850 and 740 kBq/μg, respectively. After radiolabeling, the radiochemical purity of the antibody was examined through high-performance liquid chromatography on a 5Diol-300-II column (Nakarai, Kyoto, Japan) and an isocratic mobile phase of 100 mmol/l of phosphate buffer (pH 6.8) at a flow rate of 1 ml/min.

In-vitro assay

In a cell-binding assay, serially diluted H226 cells (5×10^6 to 2×10^4 cells) or 211H cells (1×10^7 to $\times 10^6$) in phosphate-buffered saline (PBS) were incubated with the radiolabeled antibody (20 kcpm) for 1 h on ice. The cells were then centrifuged and washed twice with PBS. The radioactivity bound to the cells was counted using an auto-well gamma counter (ALOKA, Tokyo, Japan). The immunoreactivity of radiolabeled antibodies was measured according to the method of Lindmo *et al.* [15]. In a competitive inhibition assay, the radiolabeled antibody (20 kcpm) was incubated with 2×10^6 H226 cells in the presence of varying concentrations of the unlabeled antibody (0, 0.05, 0.1, 0.5, 1, 5, and 10 μg/ml) for 1 h on ice. The cells were then centrifuged and washed twice with PBS. The radioactivity bound to the cells was counted. The data were analyzed by GraphPad Prism software (Graphpad Software, La Jolla, California, USA) to determine the dissociation constants. In an internalization assay, H226 cells (2×10^6) in a culture medium were preincubated with radiolabeled antibody (20 kcpm) for 1 h at 4°C. The cells were washed once with a culture medium and collected by centrifugation. The collected cells were further cultured at 37°C or on ice in a fresh medium without radiolabeled antibodies. At various time points, the supernatant and the cells were separated by centrifugation. The supernatant was added with 10% trichloroacetic acid (Sigma) for 15 min on ice and then separated by centrifugation to determine the nonprotein-bound fraction (supernatant) and protein-bound fraction (pellet). The cells were washed with acidic buffer

[0.05 mol/l of glycine HCl (pH 2.8) and 0.1 mol/l of NaCl] for 15 min at room temperature, and were then separated by centrifugation to determine both the membrane-bound fraction (supernatant) and internalized fraction (pellet).

Biodistribution of ^{111}In-labeled or ^{125}I-labeled antibody in mouse models

Female BALB/c-nu/nu mice (5 weeks old, CLEA Japan, Tokyo, Japan) were inoculated with 4×10^6 H226 and 2×10^6 211H cells subcutaneously in the left and right thighs, respectively. As 211H cells grow faster than H226 cells in mice (~15 days difference), the inoculation day of each cell line was adjusted to ensure that the tumor xenografts were of equal size. The experiments were performed when the xenografted tumors reached a diameter of approximately 10 mm. For the biodistribution experiments, mice bearing H226 and 211H tumors were intravenously injected with a mixture of ^{111}In-labeled or ^{125}I-labeled antibodies (IgG or Fab, 37 kBq each). The injection protein dose was adjusted to 5 μg per mouse by adding the unlabeled antibody. At 24, 48, and 96 h after injection of IgG or at 1, 6, and 12 h after injection of Fab, the groups of mice (n=5 each) were killed and blood was obtained from the heart. The tumor and major organs were removed and weighed. Radioactivity was measured using the gamma counter. The data were expressed as percentage of injected dose per gram of tissues (% ID/g) normalized to a mouse with a body weight of 20 g. The statistical differences in tumor uptake were compared between H226 and 211H tumors using the Student's t-test (two-tailed). The experimental protocol was approved by the Institutional Animal Care and Use Committee of our institute, and all animal experiments were performed in accordance with the Institutional guidelines on animal care and handling.

Biodistribution and PET imaging of ^{64}Cu-DOTA-Fab

Mice bearing H226 tumor were injected with ^{64}Cu-DOTA-Fab (37 kBq in 5 μg protein). At 1, 6, and 12 h after injection of Fab, the groups of mice (n=5 each) were killed and the biodistribution was determined as described earlier. The statistical differences in tumor uptake were compared between ^{64}Cu-DOTA-Fab and ^{111}In-DTPA-Fab tumors using the Student's t-test (two-tailed). For PET experiments, a mouse bearing a H226 tumor was injected in the tail vein with approximately 4 MBq of ^{64}Cu-DOTA-Fab. At 1, 6, and 15 h post injection, the mouse was anesthetized using isoflurane and imaged using a small animal PET scanner (Inveon, Siemens Medical Solutions, Malvern, Pennsylvania, USA). The acquisition time was 30 (at 1 and 6 h) or 60 min (at 15 h), and the images were reconstructed using a three-dimensional maximum a posteriori (18 iterations with 16 subsets, β=0.2 resolution) without attenuation correction.

Results

In-vitro characterization of ^{111}In-labeled or ^{125}I-labeled IgGs and Fabs

We conducted cell binding assays with H226 (high ERC expression) or 211H (low ERC expression) cells with ^{111}In-labeled or ^{125}I-labeled IgG and Fab. Binding of 5×10^6 H226 cells to ^{111}In-DTPA-IgG, ^{125}I-IgG, ^{111}In-DTPA-Fab, and ^{125}I-Fab was 77.5, 64.0, 63.8, and 63.3%, respectively (Figs 1a and 2a), and that of 5×10^6 211H cells to ^{125}I-IgG and ^{125}I-Fab was 30.5, and 28.7%, respectively (data not shown). The immunoreactive fractions of ^{111}In-DTPA-IgG, ^{125}I-IgG, ^{111}In-DTPA-Fab, and ^{125}I-Fab were calculated as 87, 70, 82, and 64%, respectively. The results of the competitive inhibition assay revealed the dissociation constants for ^{111}In-DTPA-IgG, ^{125}I-IgG, ^{111}In-DTPA-Fab, and ^{125}I-Fab to be 7.8, 4.3, 5.0, and 8.0 nmol/l, respectively, and the number of binding sites for ^{111}In-DTPA-IgG and ^{125}I-IgG to be 6.6×10^4 and 7.5×10^4 per H226 cell, respectively (Figs 1b and 2b). We examined the temporal change in radioactivity localization of ^{111}In-labeled or ^{125}I-labeled IgG and Fab in H226 cells (Figs 1c, d and 2c, d). The cell membrane-bound fraction of ^{111}In-DTPA-IgG and ^{125}I-IgG rapidly decreased over time, and 23.6% of ^{111}In-DTPA-IgG and 16.1% of ^{125}I-IgG internalized after incubation at maximum (Fig. 1c and d). The nonprotein-bound fraction of ^{125}I-IgG in the culture medium increased over time (Fig. 1d). The internalization assay for ^{111}In-DTPA-Fab and ^{125}I-Fab showed that the internalized fraction of ^{111}In-DTPA-Fab and ^{125}I-Fab slightly increased (Fig. 2c and d), and the nonprotein-bound fraction of ^{125}I-Fab in the medium increased (Fig. 2d) similar to that of IgG. The protein-bound fraction of radiolabeled Fabs in the medium increased more than that of radiolabeled IgG (Figs 1c, d and 2c, d). When cells were incubated on ice, the membrane-bound fraction did not change and internalization was not observed for at least 3 h (data not shown).

Biodistribution of ^{111}In-labeled or ^{125}I-labeled IgGs and Fabs

The biodistribution experiments using ^{111}In-DTPA-IgG, ^{125}I-IgG, ^{111}In-DTPA-Fab, and ^{125}I-Fab were performed in nude mice bearing H226 and 211H tumors (Figs 3 and 4). ^{111}In-DTPA-IgG accumulated in H226 tumors at 5.3 ± 0.9% ID/g after 24 h and reached a peak value of 5.8 ± 0.5% ID/g at 48 h, while the tumor uptake of ^{125}I-IgG (2.5 ± 0.6% ID/g at 24 h) was lower than that for ^{111}In-DTPA-IgG and decreased over time (Fig. 3a and b). The uptake of ^{111}In-DTPA-IgG by 211H tumors (4.8 ± 1.6% ID/g at 24 h), which overall expressed lower amounts of ERC *in vitro* than H226 tumors, was comparable to that by H226 tumors at 24 h but decreased thereafter (Fig. 3a). The uptake of ^{125}I-IgG by 211H tumors also decreased over time (Fig. 3b), similar to that by H226 tumors. The uptake of ^{111}In-DTPA-IgG by H226 tumors at 96 h was significantly higher than that by

Fig. 1

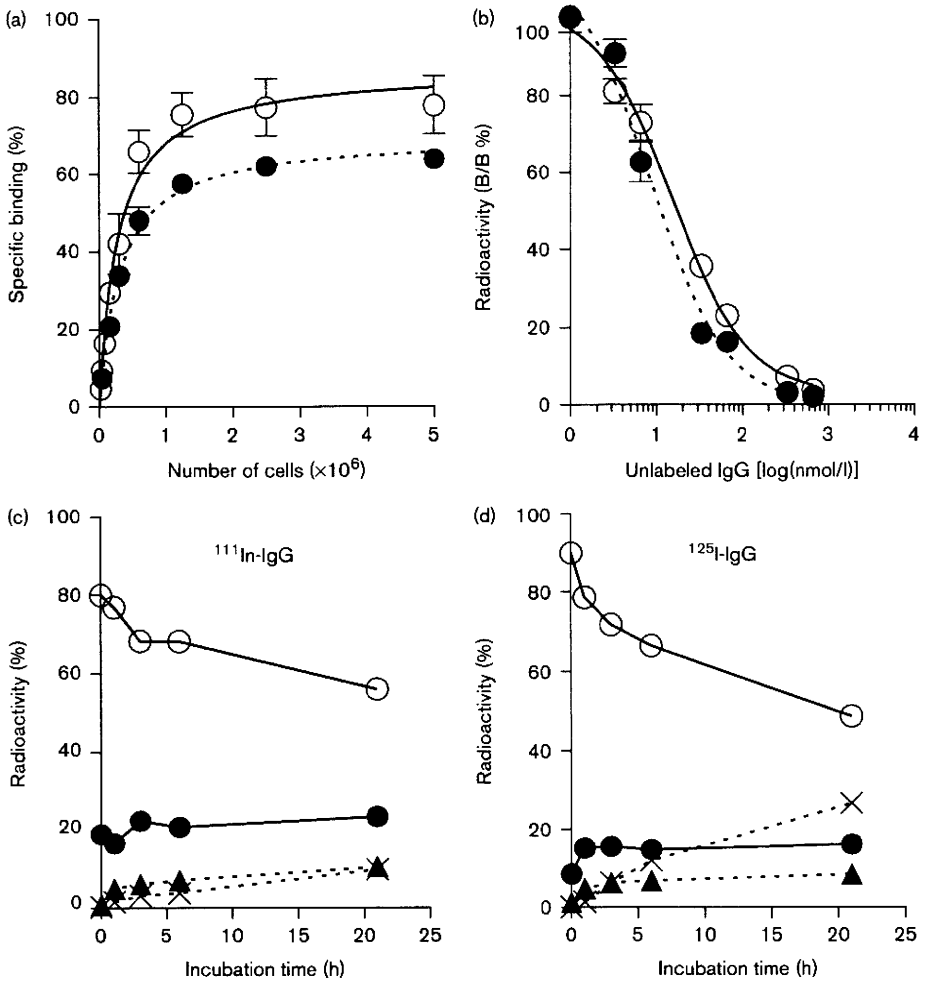

In-vitro assay for radiolabeled anti-ERC IgG in H226 cells. (a) Cell binding assay for radiolabeled IgG (open circles, ^{111}In-DTPA-IgG; closed circles, ^{125}I-IgG). Serially diluted cells were incubated with radiolabeled IgG for 1 h on ice. Cells were washed and radioactivity was counted. (b) Competitive inhibition assay for radiolabeled IgG (open circles, ^{111}In-DTPA-IgG; closed circles, ^{125}I-IgG). Radiolabeled IgG was incubated with cells in the presence of different concentrations of unlabeled IgG for 1 h on ice. Cells were washed and radioactivity was counted. Internalization assay for ^{111}In-DTPA-IgG (c) and ^{125}I-IgG (d). The radioactivity at time 0 shows the value after 1 h of preincubation with H226 cells on ice. Changes in % of total radioactivity for each fraction are plotted against incubation time at 37°C (closed circles, internalized fraction; open circles, membrane-bound fraction; closed triangles, protein-bound fraction in the culture medium, cross marks, nonprotein-bound fraction in the culture medium).

211H tumors ($P < 0.05$, Fig. 3a). The uptake of ^{111}In-DTPA-IgG by major organs was consistent with that of radiolabeled IgGs compared with other antibody–antigen combinations, as reported in earlier studies [14,16], except for the liver and kidney. The tumor-to-blood ratio of ^{111}In-DTPA-IgG was 0.8 and 0.7 at 24 h and increased to 2.4 and 1.7 at 96 h in H226 tumors and 211H tumors, respectively.

The uptake of ^{111}In-DTPA-Fab by H226 tumors was 1.6 ± 0.6, 2.1 ± 0.6, and 1.8 ± 0.2% ID/g at 1, 6, and 12 h, respectively, while that by 211H tumors was 1.2 ± 0.7, 0.9 ± 0.5, and 0.7 ± 0.2% ID/g, respectively (Fig. 4a). The uptake of ^{111}In-DTPA-Fab by H226 tumors at 1 h was similar to that for 211H tumors. However, the uptake by H226 tumors at 6 and 12 h was significantly higher than that in 211H tumors ($P < 0.01$, Fig. 4a). The uptake of ^{125}I-Fab by H226 and 211H tumors was 2.5 ± 0.7 and 2.0 ± 1.1% ID/g at 1 h, respectively, and rapidly decreased over time (Fig. 4b). Consistent with earlier studies assessing Fab labeled with radionuclide [17–20], the uptake of ^{111}In-DTPA-Fab by the kidney was extremely high, reaching a maximum of approximately 95% ID/g (Fig. 4a). The tumor-to-blood ratio of ^{111}In-DTPA-Fab in H226 tumors was 0.2, 1.3, and 2.6 at 1, 6, and 12 h, while that in 211H tumors was 0.1, 0.6, and 1.0, respectively.

Fig. 2

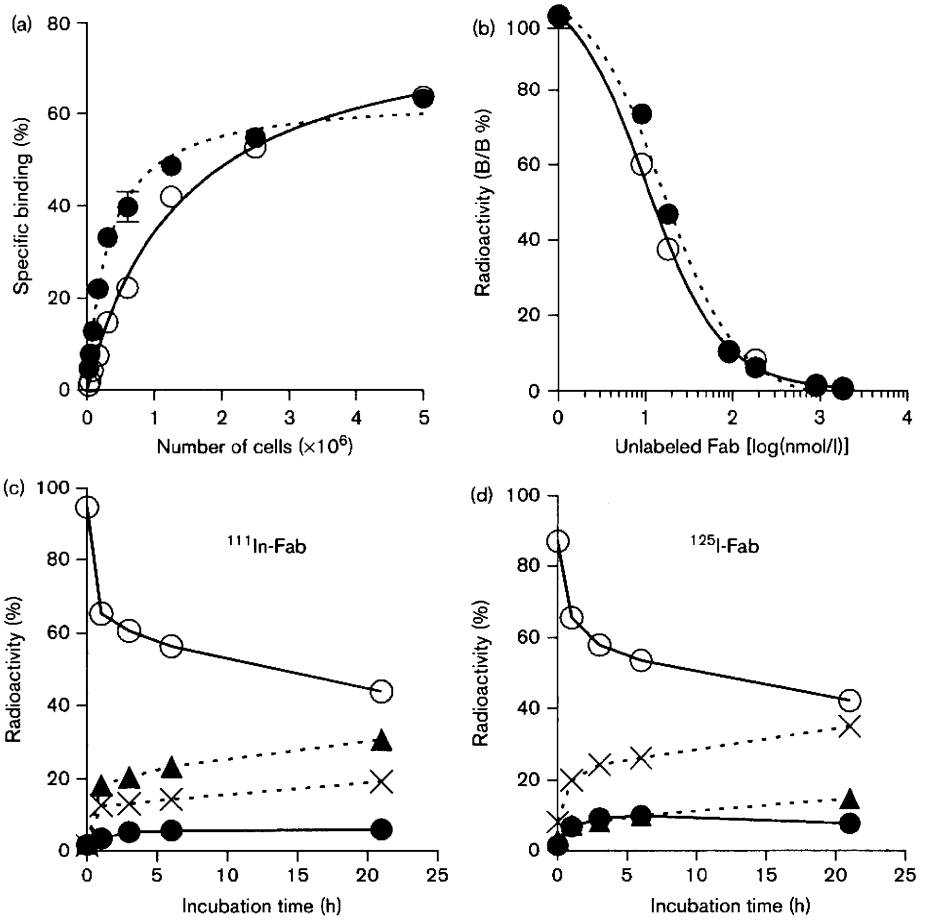

In-vitro assay for radiolabeled anti-ERC Fab in H226 cells. (a) Cell binding assay for radiolabeled IgG (open circles, ^{111}In-DTPA-Fab; closed circles, ^{125}I-Fab). (b) Competitive inhibition assay for radiolabeled Fab (open circles, ^{111}In-DTPA-Fab; closed circles, ^{125}I-Fab). Internalization assay for ^{111}In-DTPA-Fab (c) and ^{125}I-Fab (d). Changes in % of total radioactivity for each fraction are plotted against incubation time at 37°C (closed circles, internalized fraction; open circles, membrane-bound fraction; closed triangles, protein-bound fraction in the culture medium, cross marks, nonprotein-bound fraction in the culture medium).

Cell binding assay, biodistribution, and PET imaging of ^{64}Cu-DOTA-Fab

We conducted a cell-binding assay and biodistribution study of ^{64}Cu-DOTA-Fab similar to those for ^{111}In-labeled or ^{125}I-labeled Fabs. The cell-binding assay showed that binding of ^{64}Cu-DOTA-Fab to H226 cells (80.3% at 5×10^6 H226 cells) was greater than that of ^{111}In-labeled or ^{125}I-labeled Fabs, and an immunoreactive fraction of ^{64}Cu-DOTA-Fab was estimated to be 98% (Fig. 5a). In the biodistribution study, ^{64}Cu-DOTA-Fab accumulated in H226 tumors at 2.0 ± 0.2, 3.1 ± 0.2, and 2.1 ± 0.2% ID/g after 1, 6, and 12 h, respectively (Fig. 5b). These values tended to be higher than those of ^{111}In-DTPA-Fab at all time points, with a significantly higher peak value at 6 h ($P < 0.01$). The renal uptake was 54.0 ± 7.5, 57.7 ± 5.3, and 38.9 ± 2.4% ID/g after 1, 6, and 12 h, respectively; these values are lower than those of ^{111}In-DTPA-Fab. The tumor-to-blood ratio of ^{64}Cu-DOTA-Fab was 0.2, 1.2, and 2.1 after 1, 6, and 12 h, respectively, which were similar to those of ^{111}In-DTPA-Fab.

We performed serial PET imaging of ^{64}Cu-DOTA-Fab in a mouse bearing the H226 tumor at 1, 6, and 15 h after injection (Fig. 5c). The whole body radioactivity was high at 1 h, especially in the kidney, liver, and blood pool. After 6 h or more, the background activity became lower and the H226 tumor was visualized.

Discussion

The prognosis of patients with mesothelioma treated with current therapy remains poor. However, patients diagnosed at an early stage have the potential for prolonged survival. For early-stage diagnosis, image-guided biopsy combined with noninvasive imaging of a

Fig. 3

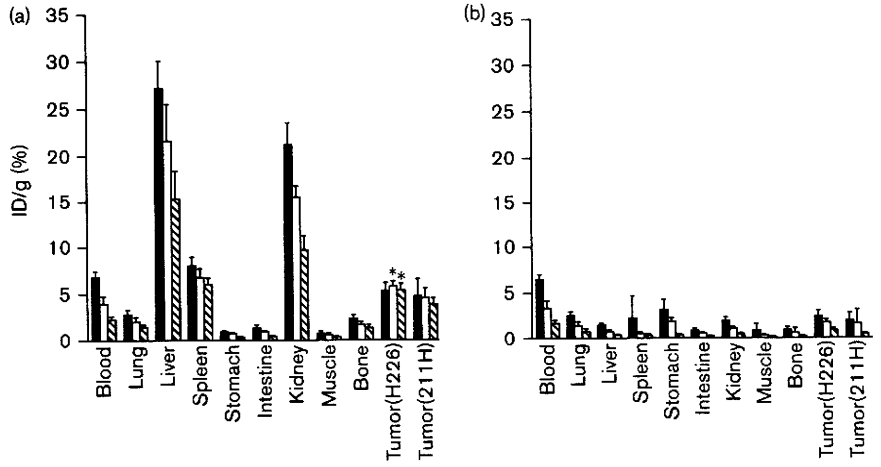

In-vivo biodistribution experiments in nude mice bearing H226 and 211H xenografts of radiolabeled IgGs. Samples were collected and weighed and radioactivity was measured at 24 (black bars), 48 (white bars), and 96 h (diagonal bars) after intravenous injection of 37 kBq each of ^{111}In-DTPA-IgG (a) and ^{125}I-IgG (b). *$P<0.05$ for *t*-tests comparing time-specific uptake of radiolabeled IgGs by H226 and 211H. ID, injected dose.

Fig. 4

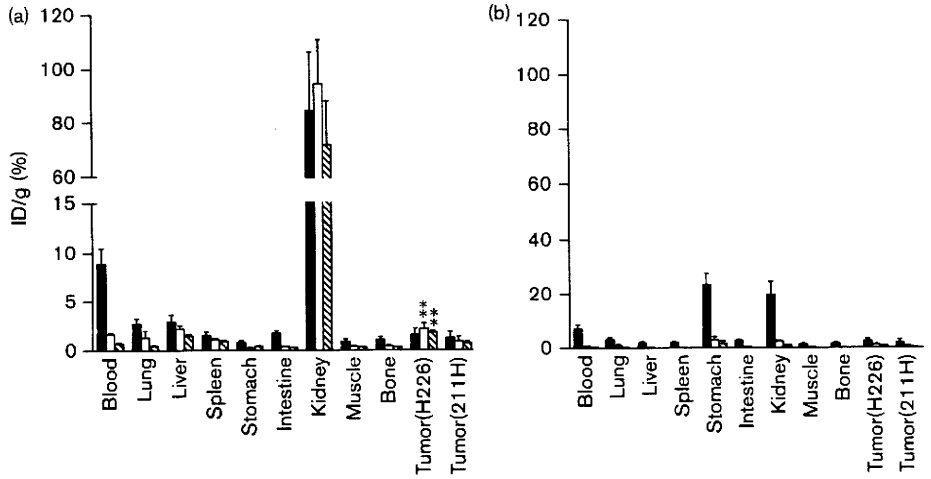

In-vivo biodistribution experiments in nude mice bearing H226 and 211H xenografts of radiolabeled Fabs. Samples were collected and weighed and radioactivity was measured at 1 (black bars), 6 (white bars), and 12 h (diagonal bars) after intravenous injection of 37 kBq each of ^{111}In-DTPA-Fab (a) and ^{125}I-Fab (b). **$P<0.01$ for *t*-tests comparing time-specific uptake of radiolabeled Fabs by H226 and 211H. ID, injected dose.

mesothelioma-specific marker would be useful. ERC is expressed in mesothelioma from an early stage and is thought to be a candidate for marker-specific imaging. In this study, we evaluated the affinity of radiolabeled monoclonal antibodies for C-ERC *in vitro* and *in vivo* for ERC-specific PET imaging.

To evaluate the radiolabeled anti-ERC antibody, we used mesothelioma cell lines and mouse xenograft models with varying degrees of ERC expression. On the basis of our earlier study, we selected the H226 cell line as a model for high ERC expression and the 211H cell line as a model for low ERC expression [12]. In this study, H226 cells showed high in-vitro binding to the anti-ERC antibody, whereas 211H cells showed lower binding. We therefore used mouse xenograft models of these two cell lines to evaluate the in-vivo biodistribution of the anti-C-ERC antibody.

According to the in-vitro study, both ^{111}In-labeled or ^{125}I-labeled IgG showed specific binding to H226 cells with high affinity. The internalization assay showed that ERC was internalized after binding with the antibody. In contrast to ^{125}I, in which free iodine formed after

Fig. 5

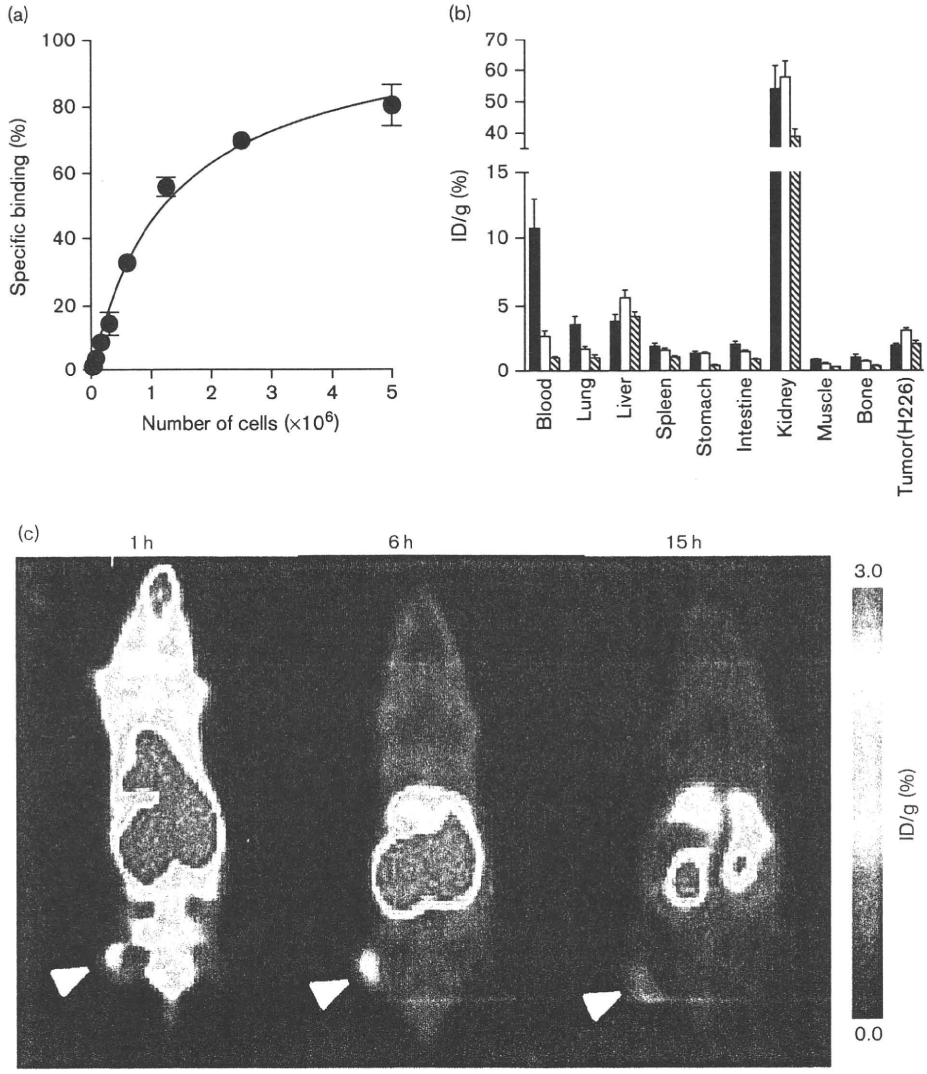

(a) Cell binding assay for ^{64}Cu-DOTA-Fab. (b) Biodistribution in nude mice bearing a H226 xenograft at 1, 6, and 12 h after intravenous injection of 0.37 MBq of ^{64}Cu-DOTA-Fab. (c) Serial positron emission tomography images of a nude mouse bearing a H226 xenografted tumor (arrowhead) at 1, 6, and 15 h after intravenous injection of 4 MBq of ^{64}Cu-DOTA-Fab. ID, injected dose.

internalization and metabolism rapidly exited the cell, ^{111}In radioactivity was retained inside the cells even after internalization. Taken together with earlier studies [14,16], these results suggest that labeling with a metal radionuclide would be suitable for ERC-specific imaging using this antibody. In fact, in-vivo biodistribution studies of ^{111}In-labeled IgG showed higher and more prolonged uptake in H226 tumors than ^{125}I-labeled IgG in mouse xenograft models, confirming the in-vitro findings mentioned above. However, as the clearance of IgG from the blood was very slow, a sufficient tumor-to-blood ratio for imaging could be obtained only at later time points, that is, 96 h.

For the detection of early-stage mesothelioma, high-sensitivity imaging is necessary and PET is the modality of choice that has the potential to meet this requisite. Most positron emitters have relatively short half-lives and are not suitable for PET imaging using IgG. Owing to its long half-life, 4.18 days, ^{124}I can be used for PET imaging with IgG. However, ^{124}I cannot be used for antibodies that undergo internalization and dehalogenation. If a positron-emitting radiometal is used, this technique requires the enhancement of the kinetics of antibodies to match the short half-lives (e.g. 12.7 h for ^{64}Cu). The use of IgG fragments such as Fab and scFv is the most popular way to expedite the clearance of antibodies [21].